Change in characteristics of a shock wave caused by interaction with turbulence

A thesis submitted in fulfillment of the requirements

for the degree of Doctor of Engineering

Kento INOKUMA

Department of Aerospace Engineering

Nagoya University

January 2020

Dissertation Committee

Koji NAGATA

Professor

Akihiro SASOH

Professor

Yasuhiko SAKAI

Professor

Atsushi MATSUDA

Professor

Acknowledgements

I would like to express my gratitude to my supervisor, Professor Koji Nagata for his constant guidance, encouragement, and support. I am blessed to meet him and to learn interest of fundamental researches. I am also grateful to Assistant Professor Tomoaki Watanabe. My research could not be completed without him. I got a lot of inspiration from him through the execution of the present study. I would like to thank Professor Yasuhiko Sakai for giving me precious comments and advice from the point of view of a turbulence researcher. I would like to thank Professor Akihiro Sasoh, who gave me valuable comments and advice based on his rich knowledge and experience for shock wave researches. I would like to thank Professor Atsushi Matsuda for reviewing my thesis. I am grateful to Associate Professor Koichi Mori for his advice and the discussions in the seminars in the laboratory.

I am also grateful to all the members of Fluid Dynamics Laboratory, Nagoya University. I am happy to communicate with them and to work hard together.

I was working as a research fellowship of Japan Society for the Promotion of Science (DC1) during my PhD period. Part of my work was supported by JSPS KAKENHI Grant No. 18J21758.

Finally, I would like to show my greatest appreciation to my family for their devoted support and understanding for my PhD journey.

Kento Inokuma

Contents

List of Published Papers

Chapter 2

Inokuma, K. et al. (2019). "Statistics of overpressure fluctuations behind a shock wave interacting with turbulence". In *Phys. Fluids* 31.8, p.085119.

Chapter 3

Inokuma, K. et al. (2017). "Finite response time of shock wave modulation by turbulence". In *Phys. Fluids* 29.5, p. 051701.

Chapter 4

Inokuma, K. et al. (2019). "Statistical properties of spherical shock waves propagating through grid turbulence, turbulent cylinder wake, and laminar flow". In *Phys. Scr.* 94.4, p. 044004.

List of Figures

List of Tables

List of Symbols

a	sound speed
A	cross-sectional area of ray tube
d	horizontal distance from pressure transducer
d_{HP}	horizontal distance from hot wire to pressure transducer
D	cylinder diameter
h	vertical distance from measurement plate
L	horizontal distance from shock tube to pressure transducer
L_u	longitudinal integral length scale of streamwise velocity
L_{ur}	lateral integral length scale of streamwise velocity
M	mesh size
M_{S}	shock Mach number
M_{S0}	Initial shock Mach number or ensemble averaged shock Mach number
M'_{S}	shock Mach number fluctuation ($M'_{\mathrm{S}} = M_{\mathrm{S}} - M_{\mathrm{S0}}$)
$M'_{\mathrm{S}l}$	M'_{S} caused when shock wave propagates along distance x_l
M_{T}	turbulent Mach number
P	overpressure
r	radial coordinate
r_0	radial length scale of turbulence in model

R	correlation coefficient
R_{SP}	distance from shock-tube end to pressure transducer
Re_D	Reynolds number based on D
Re_M	Reynolds number based on M
Re_λ	turbulent Reynolds number based on λ
t	time
t_{c}	time since shock wave arrives at pressure transducer
u	streamwise velocity fluctuation
u_{A}	propagation velocity of disturbance along shock wave surface
U	streamwise velocity
U_0	mean streamwise velocity
U_{S}	shock propagation velocity
U_{S0}	ensemble averaged shock propagation velocity
x, y, z	Cartesian coordinates
$(x_{\mathrm{A}}, r_{\mathrm{A}})$	intersection of non-deformed part of shock wave and reflected wave
$(x_{\mathrm{B}}, r_{\mathrm{B}})$	location of shock wave propagating in velocity disturbance u
$(x_{\mathrm{R}}, r_{\mathrm{R}})$	point of (x, r) on shock ray
x_l	axial length scale of turbulence in model
x_{S}	x coordinate of the shock wave surface
α	glancing incidence
γ	heat capacity ratio
Δp	peak overpressure
$\Delta p'$	peak-overpressure fluctuation ($\Delta p' = \Delta p - \langle \Delta p \rangle$)

η	Kolmogorov microscale
θ	Angle of incidence of shock wave from the vertical direction
θ_R	Angle of shock ray from x axis
λ	Taylor microscale
ν	kinematic viscosity
ξ_1	streamwise distance from cylinder center

Subscripts:

ave	time average
rms	root mean square
$\langle\ \rangle$	ensemble average taken in number of runs of experiments

Chapter 1

Introduction

1.1 Background

Shock wave is a representative phenomenon in compressible fluid dynamics, and can be found in various fields of both engineering and science. In engineering applications, shock waves can be observed around a supersonic airplane, and their influences on the aerodynamic flight performance have been discussed in terms of the effects on the wave drag (Bushnell, 2004) and on the engine performance (Gnani, Zare-Behtash, and Kontis, 2016).

One of the most important problems of shock waves is a sonic boom (Maglieri et al., 2014), which is a noise pollution caused by the shock waves generated by supersonic flight, and is known to be enormous damage for our living environment and wildlife ecosystem (Pepper, Nascarella, and Kendall, 2003). As the demand for the development of the next-generation supersonic transport increases in the recent globalization, there is an urgent need to solve the sonic boom problem. There have been some studies aimed at the reduction of the sonic boom. For example, in D-SEND and D-SEND #2 projects by JAXA, the shape of the supersonic aircraft was

studied for the realization of the low boom (Honda and Yoshida, 2012; Honda and Yoshida, 2014).

On the other hand, the pressure waveforms of the shock waves are known to be largely changed by the interaction with the atmospheric turbulence (Maglieri, 1966; Pierce, 1971; Plotkin and George, 1972; Piacsek, 2002; Yamashita and Obayashi, 2009; Jeong, Shimoyama, and Hashimoto, 2013). Since the pressure waveforms are closely related to the noise level of the sonic boom, it is necessary for us to develop the prediction and modeling of turbulence effects on the shock wave.

The change in the shock characteristics after the interaction with turbulence can also be seen in the shock-boundary layer interaction problems (Delery, 1985; Dolling, 2001; Tamba et al., 2015b; Agostini, Larchevêque, and Dupont, 2015; Ozawa, 2016; Li et al., 2017; Fang et al., 2018; Zhuang et al., 2018). It is known that the shock wave formed on a transonic airfoil induces the separation of the turbulent boundary layer on the airfoil from the shock foot to the trailing edge, which causes the unsteady motion of the shock wave (Seegmiller, Marvin, and Levy Jr., 1978; Delery, 1985). It is also known that the boundary layer formed inside the air intake of a jet engine interacts with the shock wave in the intake, resulting in the fluctuations of the total pressure behind the shock wave (Delery, 1985). Hence, the shock wave characteristics in 'shock-turbulence interaction' (Andreopoulos, Agui, and Briassulis, 2000) are very important in aeronautical engineering problems.

Another notable result in shock-turbulence interaction problems is the amplification of turbulence after the interaction with the shock wave, which can alter spatial distributions of momentum, energy, chemicals, and heat of turbulence. Therefore, the shock-turbulence interaction can have a strong influence on the mixing properties of

turbulence. Such phenomena are observed, for instance, in star formations in galaxies by supernova explosions (Mac Low and Klessen, 2004) and in the magnetic field downstream of the solar-wind termination shock, where large-scale fluctuations were confirmed (Burlaga et al., 2006; Giacalone and Jokipii, 2007). In nuclear physics, shock-turbulence interaction can be found in inertial confinement fusion (Thomas and Kares, 2012), where the characteristics of turbulent mixing past a shock wave are involved in the development or decay of the fusion.

Thus, both characteristics of the shock wave and turbulence are mutually affected, so that fundamental study for the shock-turbulence interaction has a large potential for understanding the phenomena and for the application to more efficient aeronautical products.

1.2 Previous studies on shock-turbulence interaction

1.2.1 Laboratory experiments

There have been some laboratory experiments on shock-turbulence interaction for the fundamental research of both characteristics of the turbulence and the shock wave. For the investigation of the shock wave effects on turbulence, Keller and Merzkirch, 1994 visualized the density field of compressible turbulence in shock tube experiments by using the speckle method, where the flow past a grid interacts with a shock wave reflected at the tube end. They found that the root-mean-squared (rms) density fluctuations, the integral length scale, and the Taylor microscale of density fluctuations are increased after the interaction with the shock wave. Barre, Alem, and

Bonnet, 1996 conducted experiments on high Mach-number quasi-isotropic turbulence interacting with a standing shock wave, where they discovered the increase in the rms velocity fluctuation and the decrease in the longitudinal integral length scale of the velocity fluctuations. Poggi, Thorembey, and Rodriguez, 1998 studied turbulent characteristics of gaseous mixtures of SF_6 and air induced by Richtmyer-Meshkov instability in shock tube experiments. They measured velocity fluctuations affected by the shock wave by using laser Doppler anemometry. Agui, Briassulis, and Andreopoulos, 2005 also performed shock tube experiments on the interaction between a shock wave and compressible turbulence, where they measured velocity characteristics of turbulence with a multi-hot-wire probe before and after interaction with a shock wave. They reported that in the shock-normal direction, the rms velocity fluctuation is increased, and the longitudinal integral length scale and the Taylor microscale are decreased after the interaction, while the changes in such velocity characteristics are small in the shock-tangential direction. The increase in the rms velocity fluctuation and the decrease in the longitudinal integral length scale were also reported in the experimental study on the interaction between a weak spherical shock wave and low Mach-number grid turbulence (Kitamura et al., 2017).

The effects of turbulence on the shock wave characteristics have also been studied. Dosanjh, 1956 conducted shadowgraph visualization in the shock-tube experiments of the interaction between a planar shock wave and turbulence, where they found that the shock wave front is fluctuated by the interaction. Experiments on interaction between a blast wave and a slit jet were also conducted (Lipkens and Blackstock, 1998a; Lipkens and Blackstock, 1998b). They investigated the characteristics

of overpressure behind the blast wave interacting with the jet, such as peak overpressure and rise time required for the overpressure to reach a peak value. Their work revealed that the fluctuations of both peak overpressure and rise time are increased with the jet velocity or with the length of turbulence, and that the relative intensity of those fluctuations are increased with the shock propagation distance. Kim, Sasoh, and Matsuda, 2010 also experimentally studied the interaction between a blast wave and a jet, where they investigated the relation between the shock front geometry and the overpressure modulation behind the shock caused by turbulence. They found the peak overpressure is increased when the shock wave front is locally flattened. Sasoh et al., 2014 conducted wind tunnel experiments on interaction between a weak spherical shock wave and grid turbulence. Such quasi-homogeneous isotropic turbulence as grid turbulence enabled them to independently investigate the effects of velocity fluctuation on the shock characteristics apart from the effect of an inhomogeneous mean velocity profile. They showed that the peak overpressure fluctuation intensity linearly increases with the rms velocity fluctuation of turbulence. In the recent study by Tamba et al., a counter-driver shock tube was developed for the shock-turbulence interaction study, where the strength of the shock wave and that of turbulence can be independently set (Tamba et al., 2015a). From their shadowgraph visualization of the shock wave, they found that the deformation of the shock wave front becomes larger with the larger relative strength of turbulence to shock wave (Tamba et al., 2019).

1.2.2 Numerical simulations and theories

Numerical and theoretical studies have mainly been performed for the interaction between a planar shock wave and homogeneous isotropic turbulence for the simplification of the shock-turbulence interaction phenomena. This is important for understanding the basic elements of the phenomena. Most numerical studies have focused on the change in the turbulence characteristics after the interaction. The amplification of the turbulent kinetic energy after the interaction were reported in numerical simulations and theories (Lee, Lele, and Moin, 1993; Larsson and Lele, 2009; Donzis, 2012a; Ryu and Livescu, 2014; Kitamura et al., 2016; Tanaka et al., 2018; Chen and Donzis, 2019). Larsson and Lele, 2009 found that the Kolmogorov microscale decreases, the vorticity variance increases, and the Reynolds stresses becomes anisotropic by the interaction. Linear interaction analysis and direct numerical simulations by Ryu and Livescu, 2014 showed that the topology of the turbulent structure is changed past shock wave.

Remarkable findings related to the change in the shock wave characteristics by turbulence have also been obtained by numerical and theoretical studies. The attenuation of the shock wave strength by the interaction with turbulence was confirmed in the theoretical study by Lele, 1992. The numerical simulations by Lee, Lele, and Moin, 1993 found that a clear shock wave front can disappear in the case of the interaction between strong turbulence and a weak shock wave. The similar phenomenon was also observed in other previous studies (Larsson and Lele, 2009; Larsson, Bermejo-Moreno, and Lele, 2013), where the existence of 'shock holes' or local disappearance of jumps in physical quantities across the shock wave was confirmed. When a large part of the shock surface is occupied by the shock holes, this shock

wave is called a broken shock wave. The condition under which the shock wave is broken by interaction with turbulence was investigated numerically (Larsson and Lele, 2009; Larsson, Bermejo-Moreno, and Lele, 2013) and theoretically (Donzis, 2012b). Larsson, Bermejo-Moreno, and Lele, 2013 showed that density jump across the shock wave is correlated with the streamwise shock position variance caused by the shock wave deformation. Recently, Sethuraman and Sinha, 2020 performed direct numerical simulations and linear interaction analysis on the effects of incoming turbulence strength on the fluctuations in thermodynamic quantities such as pressure, density, temperature, and entropy downstream of the shock wave. They found that such thermodynamic variances past the shock wave increase with the turbulent Mach number for a fixed shock Mach number.

1.3 Objective and structure of this thesis

From the important findings of the previous studies on the shock-turbulence interaction, this thesis picks up the statistical properties of the fluctuations of the overpressure behind the shock wave induced by the interaction with velocity fluctuations of turbulence. There are various factors of turbulence that can be important in the interaction with the shock wave. In some situations, temperature fluctuations in turbulence induced by compressibility or other flow conditions can be important since the speed of sound is directly related to temperature. All turbulent flows should have velocity fluctuations, whose influence is, therefore, essential in turbulent effects on the shock wave. Therefore, the thesis focuses on the effects of velocity fluctuations

on the shock wave. On the other hand, since few experimental studies have considered the shock wave and turbulence strength parametrically, the systematical data have not been obtained adequately for the investigation of the dependence of shock wave statistics on the conditions of the shock wave and turbulence. In the inner-shock tube experiments conducted in various previous studies, the shock-turbulence interaction can easily be formed, however, the repetition of the interaction experiments needed for the statistical analyses have been limited due to the structure of the diaphragm. Moreover, the turbulent flow generated in the shock tube often has temperature fluctuations due to compressibility effects, and it is difficult to investigate effects of velocity fluctuations independently from those of temperature. It is also difficult to evaluate the turbulence conditions correctly since the sampling time for the turbulence measurement obtained at one run of each interaction experiment is dependent on the shock tube system. Numerical studies are advantaged to obtain such statistics, however, most of them have considered compressible turbulence, where the thermodynamic fluctuations are significant, so that the effect of the velocity fluctuations on the shock wave statistics has not been identified.

It is also important to understand the mechanism of how the velocity fluctuations of turbulence induce the overpressure fluctuation behind the shock wave. The process of the interaction can be studied if both instantaneous velocity and overpressure are accessible. However, most experimental studies conducted measurement of one of turbulence or shock wave.

It should also be mentioned that most previous studies treated homogeneous turbulence for the interaction problems because of the simplification of the phenomena. For the next step, it is of interest to investigate how the inhomogeneity of turbulence

affects the shock wave. Some previous experiments treated inhomogeneous turbulence such as jet, however, they did not focus on the effects of the inhomogeneity on the shock wave characteristics.

In this thesis, to solve the above questions, repetitive shock-turbulence interaction experiments are conducted by using a diaphragm-less shock tube and a wind tunnel, and the statistics are systematically investigated for the shock wave after the interaction with homogeneous or inhomogeneous turbulence with a low turbulent Mach number, where turbulence itself does not have compressibility effects. The same shock wave generator is used throughout the experiments conducted in this thesis while various turbulence conditions are considered depending on the purpose.

In Chapter 2, wind tunnel experiments on the interaction between a shock wave and grid turbulence with a low turbulent Mach number are reported, where the intensities of the shock wave and turbulence are varied. The dependence of the overpressure behind the shock wave on the shock Mach number and turbulent Mach number is evaluated, and compared with a theoretical model developed based on the shock wave geometry. The model is also used to discuss the presence of the shock holes and criterion for broken shock wave.

In the study in Chapter 3, simultaneous measurements of the turbulence velocity and the overpressure behind the shock wave are conducted for the shock wave propagating in the grid turbulence with the same experiential set up as in Chapter 2. The correlation between the instantaneous velocity and the overpressure is discussed. The theoretical model developed in Chapter 2 is also considered for the explanation of the experimental results.

In Chapter 4, the interaction between cylinder wakes and the shock wave is investigated with the same wind tunnel facility, where the effects of inhomogeneity of turbulence on shock wave overpressure characteristics are investigated. The effects of the inhomogeneity on the shock wave modulation are compared with that of the homogeneous turbulence.

Chapter 2

Statistics of overpressure fluctuations behind a shock wave interacting with turbulence

2.1 Introduction of this chapter

In the previous numerical simulations, it was found that the shock wave propagation in turbulence can result in the shock holes, which are locally broken regions of the shock wave, across which jumps in physical quantities do not exist (Lee, Lele, and Moin, 1993; Larsson and Lele, 2009; Larsson, Bermejo-Moreno, and Lele, 2013). Numerical studies (Lee, Lele, and Moin, 1993; Larsson and Lele, 2009; Larsson, Bermejo-Moreno, and Lele, 2013; Tanaka et al., 2018) and a theoretical study (Donzis, 2012b) have been attempted to find parameters that characterize the influence of turbulence on the shock wave. These previous studies have considered the shock Mach number $M_{S0} = U_{S0}/a_0$, turbulent Mach number $M_T = \sqrt{2k_T}/a_0$, and turbulent Reynolds number $Re_\lambda = u_{rms}\lambda/\nu$ as dominant parameters in the turbulence

effects on the shock wave, where a_0 is the speed of sound in front of the shock wave, U_{S0} is the propagation speed of the shock wave, k_T is the turbulent kinetic energy, u_{rms} is the root-mean-squared (rms) velocity fluctuation, λ is the Taylor microscale, and ν is the kinematic viscosity. For example, previous numerical and theoretical studies have proposed various criteria under which the shock holes appear. It is suggested that the shock holes appear when $M_T^2/(M_{S0}^2-1) \gtrsim 0.1$ in Lee, Lele, and Moin, 1993, $M_T^2/(M_{S0}^2-1) \gtrsim 0.06$ in Larsson and Lele, 2009 and $M_T/(M_{S0}-1) \gtrsim 0.6$ in Donzis, 2012b and Larsson, Bermejo-Moreno, and Lele, 2013. The non-dimensional parameters $M_T/(M_{S0}-1)$ and $M_T^2/(M_{S0}^2-1)$, considered as the measure of the relative strength of turbulence to the shock wave, are often used to understand the interaction between turbulence and the shock wave (Lee, Lele, and Moin, 1993; Larsson and Lele, 2009; Donzis, 2012b; Larsson, Bermejo-Moreno, and Lele, 2013; Tanaka et al., 2018). However, so far, there are no consensuses on non-dimensional parameters that characterize the turbulence effects on the shock wave. Donzis, 2012b theoretically indicated that the variance of the fluctuation in the dilatation of the shock wave normalized by the mean dilatation increases with $M_T/(M_{S0}-1)$. Here, the dilatation is defined as the minimum velocity gradient in the shock propagation direction, which represents the discontinuity and strength of the shock wave. The dilatation fluctuation was estimated from the ratio of the velocity jump across the shock wave and shock thickness fluctuation in the analysis, where the fluctuations of the velocity jump are ignored. However, the fluctuations of the pressure jump, that is closely related to the fluctuations of the velocity jump by the Rankine-Hugoniot relations, were confirmed in previous studies (Lipkens and Blackstock, 1998b; Lee, Lele, and Moin, 1993; Larsson, Bermejo-Moreno, and Lele, 2013; Sasoh et al., 2014;

Tanaka et al., 2018). Numerical simulations have shown that the turbulent velocity fluctuation in the shock normal direction has correlation with the fluctuation of the overpressure behind the shock wave at a low turbulent Mach number (Tanaka et al., 2018). It is therefore important to experimentally and theoretically examine the relation between these parameters and the jump in physical variables across the shock wave.

In the present study, experiments are conducted for the interaction between a weak spherical shock wave and grid turbulence. A spherical shock wave is one of the canonical shock waves, and it has been extensively studied by theories, experiments, and numerical simulations (Landau, 1945; Chisnell, 1957; Whitham, 1958; Friedlander, 1946; Needham, 2010; Liang, Wang, and Chen, 2002). A weak shock wave is expected to be suitable for the investigation of the parameters $M_T/(M_{S0}-1)$ and $M_T^2/(M_{S0}^2-1)$ since the difference between these two parameters becomes large for such a shock wave with $M_{S0} \approx 1$. The interaction between a weak shock wave and turbulence is also important in various problems. For example, the shock wave in the sonic boom problem is weak at the ground level, and the measured overpressure is of order of 10^1 to 10^2 Pa (Carlson, 1967). Predictions of the sonic boom caused by the shock wave during the supersonic flight need models for the influences of the atmospheric turbulence on the shock wave (Pierce, 1971).

The purpose of this chapter is to experimentally and theoretically assess the non-dimensional parameters that characterize the effects of turbulent velocity fluctuations on the shock wave characteristics. A shock deformation model is proposed for the investigation of the turbulence effects on the shock wave. The shock deformation model can also be used for the explanation of the response time of the overpressure

modulation of the shock wave by turbulence, which is addressed in Chapter 3. The model considers the shock wave deformation caused by a non-uniform velocity profile. The model is extended to investigate the shock Mach number fluctuation caused by the deformation: following the approximate theory by Whitham, 1957, the present model obtains the local shock Mach number fluctuation from the change in the ray tube area associated with the deformation. The present model is compared with the experimental results of the statistics of the overpressure fluctuation behind the shock wave.

2.2 Experimental methods

2.2.1 Experimental setup

Experiments are conducted for the interaction between a spherical shock wave and grid turbulence in a wind tunnel for various values of M_{T} and M_{S0} in order to cover a wide range of $M_{\mathrm{T}}/(M_{\mathrm{S0}}-1)$ and $M_{\mathrm{T}}^2/(M_{\mathrm{S0}}^2-1)$. Here, the present experiments are restricted to grid turbulence at a low turbulent Mach number (incompressible turbulence) to prevent fluctuations of thermodynamic properties from affecting the shock wave. Because grid turbulence is a good approximation of homogeneous isotropic turbulence, the influence of mean velocity gradients does not exist unlike in free shear flows (Kim, Sasoh, and Matsuda, 2010).

Figure 2.1(a) and (b) show the schematic and side view of the experimental setup, respectively. The wind tunnel and the shock generator used in this study are the same as those in the previous studies (sasoh2014statistical,kitamura2017changes). A square grid with a mesh size of M (a solidity of 0.36) is installed at the entrance to the

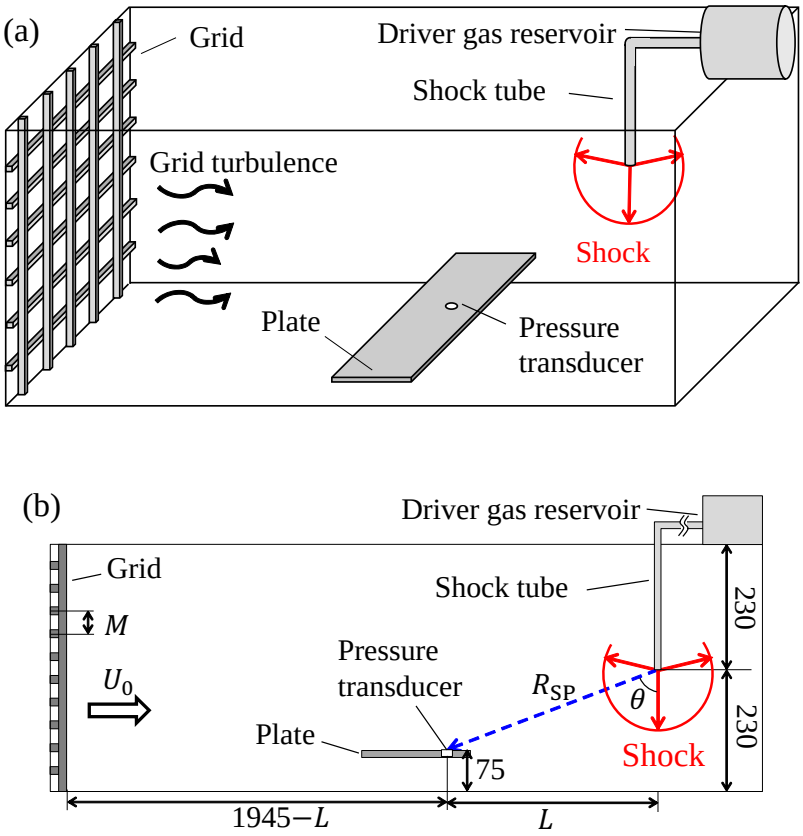

FIGURE 2.1: (a) Schematic and (b) side view of experimental setup. Lengths are shown in mm.

test section. The schematic of the grid and the definition of M are shown in Fig. 2.2. Grid turbulence with the mean streamwise velocity of U_0 develops behind the grid. The detailed properties of the grid turbulence in the present wind tunnel are reported in Kitamura et al., 2014. The shock wave is produced with the shock generator based on a quick piston, which is controlled with solenoid valves SV1 and SV6 (SMC, VG342R-06-6G-06N), and SV2 to SV5 (SMC, AV2000-N02G-6DZ) (see Fig. 2.3). By opening SV2 to SV5, dry air of 900 kPa flows into the driver gas reservoir and the rear of the piston. SV6 is used for the minute adjustment of the driver gas pressure. When SV1 is opened, the driver gas is released into the driven gas in the shock tube (air of ambient pressure). The total length and the inner diameter of the tube are 3.4

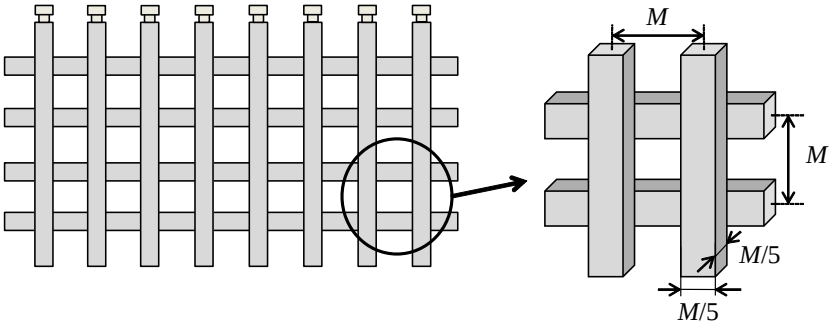

FIGURE 2.2: Schematic of grid.

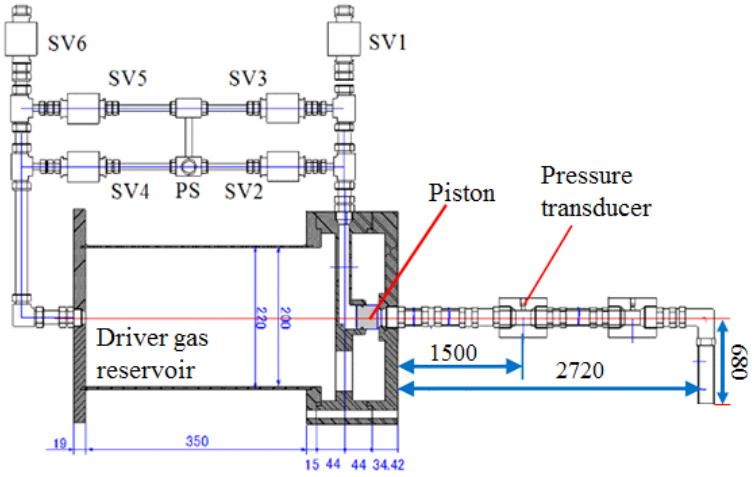

FIGURE 2.3: Schematic of the shock generator. Lengths are shown in mm.

m and 23.3 mm, respectively. After the shock wave is ejected from the open end of the shock tube, it spherically spreads and propagates in the grid turbulence developed in the test section. A pressure transducer (PCB Piezotronics Inc., 113B27) mounted on the horizontal plate is used for the overpressure measurements. The measurement plate is fixed 75 mm above the wall of the wind tunnel to prevent the boundary layer from affecting the measurements. The pressure transducer is mounted near the edge of the plate so that the pressure measurement is not affected by the growth of the Mach stem. The rise time of the pressure transducer is less than 1 μs. The resolution of the pressure measurements by our pressure transducer is 0.007 kPa. Pressure

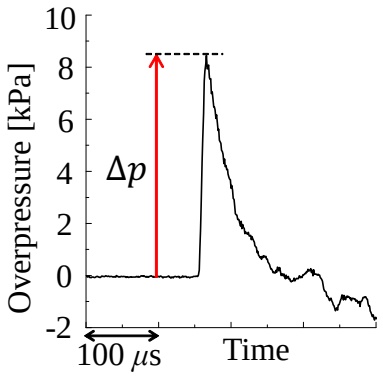

FIGURE 2.4: Example of the time history of the overpressure for case 1.

transducers with similar performance have been used for the overpressure measurements in the experiments on shock/turbulence interactions (e.g., Sasoh et al., 2014 and Kim, Sasoh, and Matsuda, 2010). Sasoh et al., 2014 used the same experimental facility, and measured the overpressure with the pressure transducer with the same resolution as in this thesis. In their study, the overpressure fluctuations caused by turbulence were well resolved for the investigations of the turbulence effects on the histogram of overpressure fluctuations, averaged overpressure, and rms overpressure fluctuations (Sasoh et al., 2014). The pressure signals are sampled at a frequency of 1 MHz with an oscilloscope (YOKOGAWA, DL850E), where the sampling is started before the shock wave is ejected.

The experiments are conducted for eight conditions shown in Tab. 2.1, which are considered by changing M, U_0, and the streamwise location of the pressure measurements, which is shown as the streamwise distance L from the open-end of the shock tube to the pressure measurement location. For each case, 400 runs of the shock wave ejections are conducted to take ensemble average, which is denoted by $\langle\ \rangle$. Figure 2.4 shows an example of the time history of the overpressure for case 1 with the definition of the peak overpressure Δp observed upon the arrival of the shock wave.

The overpressure sharply rises by the arrival of the shock wave and gradually decays with time because of an expansion wave that follows the shock wave. This waveform is typical for a spherical shock wave and similar to those obtained in previous studies (Needham, 2010; Lipkens and Blackstock, 1998b; Kim, Sasoh, and Matsuda, 2010; Salze et al., 2014; Liang, Wang, and Chen, 2002).

2.2.2 Estimation of shock Mach number

The estimation of the shock Mach numbers M_{S0} of the present experimental conditions shown in Tab. 2.1 is described here. It should be noted that Δp is the peak overpressure behind the shock wave reflected on the plate with the angle of incidence θ. Here, θ is the angle of the shock ray from the vertical direction. According to Lahiri and Ho, 2011 and Schwer, 2017, Δp measured at the pressure transducer can be represented as

$$\Delta p(\theta) = \Delta p(90^\circ)(1 + \cos\theta - 2\cos^2\theta) + \Delta p(0^\circ)\cos^2\theta. \tag{2.1}$$

For a weak shock wave ($M_{S0} \to 1$) as used in the present experiments, Eq. (2.1) can be simplified as

$$\Delta p(\theta) = \frac{1}{2}(\cos\theta + 1)\Delta p(0^\circ), \tag{2.2}$$

where $\Delta p(0^\circ) = 2\Delta p(90^\circ)$ is used according to the Rankine-Hugoniot relations for $M_{S0} \to 1$. Equation (2.2) represents the linear wave reflection at free end. The shock ejections are tested for four different θ at $L = 540$ [mm] without flow ($U_0 = 0$ [m/s]). Figure 2.5 (a) plots $\langle \Delta p \rangle$ against θ, which agrees well with Eq. (2.2). Since Eq. (2.1)

is for the case of regular reflection (Schwer, 2017), it can be confirmed that the pressure measurements in the present study are not affected by complex reflection phenomena such as Mach reflection, in which the geometry of the incident and reflected shock waves and the relation between the overpressure behind them are different from those for the regular reflection (Ben-Dor, 1992).

According to the Rankine-Hugoniot relations, the relation between $\Delta p(\theta)$ and the shock Mach number behind the shock wave reflected at the wall, $M_{\mathrm{S0R}}(\theta)$ is

$$\langle \Delta p(\theta) \rangle = \frac{2\gamma p_0}{\gamma+1}(M_{\mathrm{S0R}}^2(\theta)-1), \tag{2.3}$$

where p_0 is the mean pressure in front of the shock wave and γ is the heat capacity ratio. From Eqs. (2.2) and (2.3), the shock Mach number behind incident shock wave M_{S0} can be estimated as

$$M_{\mathrm{S0}} = M_{\mathrm{S0R}}(0) = \sqrt{1+\frac{\gamma+1}{\gamma p_0}\frac{\langle \Delta p(\theta) \rangle}{\cos\theta+1}}. \tag{2.4}$$

Figure 2.5 (b) plots M_{S0} against θ. The uncertainty of M_{S0} estimation caused by changing θ is of order of 10^{-4}, and the estimation does not seem to be dependent on θ. Here, the shock Mach number of each shot of shock wave, M_{S} is

$$M_{\mathrm{S}} = \sqrt{1+\frac{\gamma+1}{\gamma p_0}\frac{\Delta p(\theta)}{\cos\theta+1}}. \tag{2.5}$$

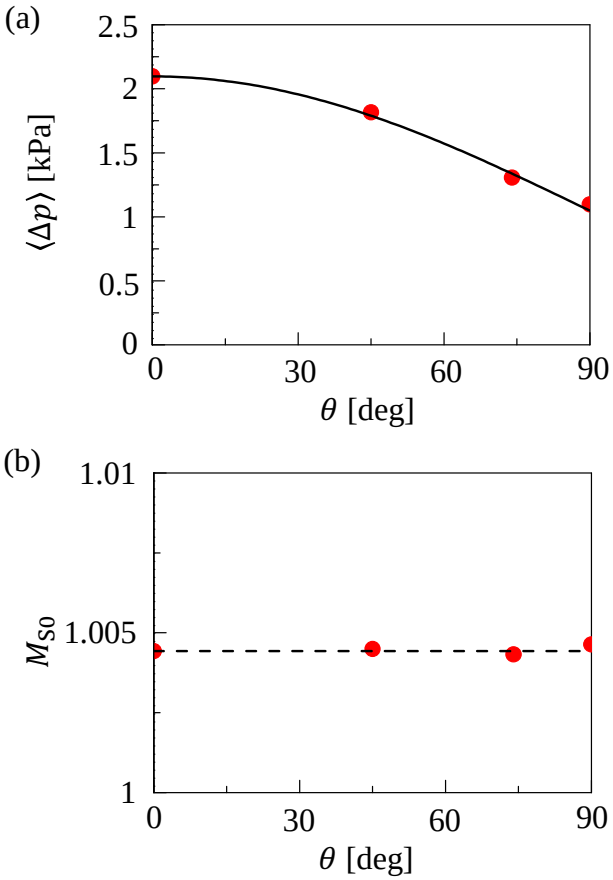

FIGURE 2.5: (a) $\langle \Delta p \rangle$ plotted against θ. Black solid line shows Eq. (2.2). Plots are obtained at $L = 540$ [mm] for the shock waves propagating in the test section without flow. (b) M_{S0} estimated from $\langle \Delta p(\theta) \rangle$ and Eq. (2.4) plotted against θ. Broken line shows $M_{S0R}(0)$.

By considering the zero- and first- order terms of the Taylor series of Eq. (2.5), one can obtain the following equation:

$$M_S \approx M_{S0} + \frac{\gamma+1}{2\gamma M_{S0}^2} \frac{\Delta p'}{p_0(\cos\theta + 1)}, \tag{2.6}$$

where $\Delta p' = \Delta p - \langle \Delta p \rangle$. The overpressure fluctuation is $\Delta p'/p_0 = O(10^{-4})$ in each shot, therefore, according to Eq. (2.6), the shock Mach number fluctuation in each shot, $M_S' = M_S - M_{S0}$ is of $O(10^{-4})$. Hence, the shock Mach numbers M_{S0} shown in Tab. 2.1 are estimated with $\langle \Delta p \rangle$ by considering Eq. (2.4).

2.2.3 Characteristics of grid turbulence

Streamwise velocity measurements by hot wire anemometry (DANTEC DYNAMICS, Streamline) with an I-type hot wire probe (DANTEC DYNAMICS, 55P11) are conducted in grid turbulence. Statistics of the streamwise velocity are computed with a time average denoted with subscript $*_{\mathrm{ave}}$. Table 2.1 summarizes the characteristics of the grid turbulence at the same streamwise location as the pressure transducer. As examples of the velocity measurements, Figs. 2.6 (a) to (c) show the velocity characteristics of grid turbulence for $M = 100$ [mm] at $U_0 = 10$ and 20 [m/s] as a function of the streamwise distance from the grid, x_1. The measurements are repeated three times for each point of x_1, where the measurement errors are within 1% for the calculation of the velocity characteristics. Figure 2.6 (a) shows the streamwise velocity variance $u_{\mathrm{rms}}^2 = (U^2 - U_{\mathrm{ave}}^2)_{\mathrm{ave}}$ divided by U_{ave}^2, $(u_{\mathrm{rms}}/U_{\mathrm{ave}})^2$. $(u_{\mathrm{rms}}/U_{\mathrm{ave}})^2$ is known to decay with the following power law (Krogstad and Davidson, 2010):

$$\frac{u_{\mathrm{rms}}^2}{U_{\mathrm{ave}}^2} = n_0 \left(\frac{x_1}{M} - \frac{x_0}{M} \right)^{n_{\mathrm{K}}}. \tag{2.7}$$

n_0, x_0, and n_{K} are determined by the nonlinear least-square method as conducted in Kitamura et al., 2014. The power laws calculated for the grid turbulence of the present study are $(u_{\mathrm{rms}}/U_{\mathrm{ave}})^2 = 0.059(x_1/M - 2.5)^{-1.1}$ for $U_0 = 10$ [m/s] and $(u_{\mathrm{rms}}/U_{\mathrm{ave}})^2 = 0.071(x_1/M - 2.2)^{-1.1}$ for $U_0 = 20$ [m/s], where the virtual origins x_0/M are 2.5 and 2.2, respectively. The decay exponent $n_{\mathrm{K}} = -1.1$ agrees with previous experiments (Kitamura et al., 2014) for a similar range of x_1/M.

Figure 2.6 (b) shows the Taylor microscale λ, which is defined as

$$\lambda^2 = \frac{u_{\mathrm{rms}}^2}{U_{\mathrm{ave}}^2 (\partial u/\partial t)_{\mathrm{ave}}^2}, \tag{2.8}$$

where the Taylor's hypothesis is used to replace spatial derivative $\partial/\partial x_1$ in the denominator in the original definition of λ with time derivative. λ is known to increase with the following power law (Krogstad and Davidson, 2010):

$$\frac{\lambda^2}{M^2} = \frac{10}{n_{\mathrm{K}} Re_M} \left(\frac{x_1}{M} - \frac{x_0}{M} \right). \tag{2.9}$$

Black and red lines in Fig. 2.6(b) are obtained with Eq. (2.9) for U_0 = 10 [m/s] and 20 [m/s], respectively, which agree well with the present experimental results. x_0/M in the present experiments are obtained as 2.0 and -6.7 for U_0 = 10 [m/s] and 20 [m/s], respectively.

The Taylor's hypothesis is also applied to the calculation of the longitudinal integral length scale L_u as

$$L_u = \int_0^\infty \frac{[u(x_1)u(x_1 + U_{\mathrm{ave}}t)]_{\mathrm{ave}}}{u_{\mathrm{rms}}^2(x_1)} U_{\mathrm{ave}} \mathrm{d}t. \tag{2.10}$$

As in the previous study of grid turbulence (Krogstad and Davidson, 2010; Kitamura et al., 2014), L_u increases with a power law of $(x/M - x_0/M)$. The nonlinear least-square method yields $L_u/M = 0.089(x_1/M - 1.5)^{0.69}$ for U_0 = 10 [m/s] and $L_u/M = 0.086(x_1/M - 1.3)^{0.74}$ for 20 [m/s], respectively.

The turbulent Mach number is defined with $M_{\mathrm{T}} = \sqrt{3} u_{\mathrm{rms}}/a_0$ in isotropic turbulence. The same definition is also used for the grid turbulence in this thesis because

the rms values of streamwise and transverse velocity fluctuations are close to each other (Kitamura et al., 2014). At the pressure transducer location, M_T changes depending on M, U_0, and L while the shock Mach number M_{S0} depends on L because of the decay of M_{S0} with the propagation of the spherical shock wave.

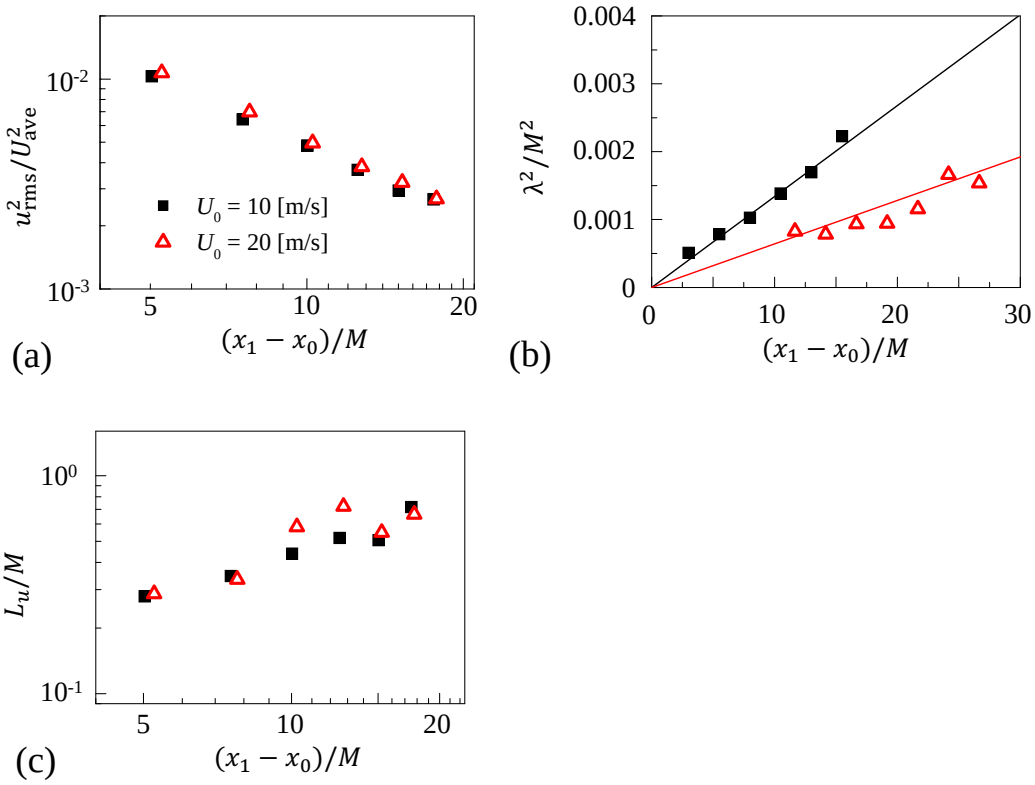

FIGURE 2.6: (a) $(u_{rms}/U_{ave})^2$, (b) $(\lambda/M)^2$, and (c) L_u/M plotted against $(x_1 - x_0)/M$ for $M = 100$ [mm] at $U_0 = 10$ and 20 [m/s]. Black and red lines in (b) are obtained with Eq. (2.9).

2.3 Experimental results

2.3.1 Averaged peak overpressure

Figure 2.7 plots $\langle \Delta p \rangle$ against the distance between the open end of the shock tube and pressure measurement location, $R_{SP} = \sqrt{L^2 + 155^2}$ [mm]. According to Landau, 1945, $\langle \Delta p \rangle$ of a spherical shock wave decays with R_{SP} as $\langle \Delta p \rangle \propto 1/(R_{SP}\sqrt{\ln(R_{SP}/k_1)})$,

TABLE 2.1: Experimental conditions. $Re_M = U_0 M/\nu$ is the grid Reynolds number. $u_{\rm rms}$, $M_{\rm T}$, and $M_{\rm S0}$ are values at the pressure measurement location ($1945 - L$ [mm] behind the grid).

Case	1	2	3	4	5	6	7	8
M [mm]	15	50	100	50	100	100	100	100
U_0 [m/s]	10	10	10	10	10	10	20	20
$Re_M \times 10^{-4}$	0.98	3.3	6.5	3.4	6.7	6.5	13	13
L [mm]	155	155	155	540	540	1000	1000	1445
$u_{\rm rms}$ [m/s]	0.141	0.316	0.545	0.377	0.636	0.850	1.76	3.20
$M_{\rm T} \times 10^4$	7.12	15.9	27.4	19.0	32.0	42.8	88.7	161
$M_{\rm S0}$	1.021	1.021	1.021	1.004	1.004	1.002	1.002	1.001

where k_1 is a constant. The least square method applied to $\langle \Delta p \rangle$ in present study yields $\langle \Delta p \rangle = 830/(R_{\rm SP}\sqrt{\ln(R_{\rm SP}/179)})$ [kPa]. The changes in $\langle \Delta p \rangle$ in cases with a same $R_{\rm SP}$ are less than 2 % despite that they have different turbulence conditions, confirming that the difference in $M_{\rm T}$ considered in our experiments does not have large effects on $\langle \Delta p \rangle$.

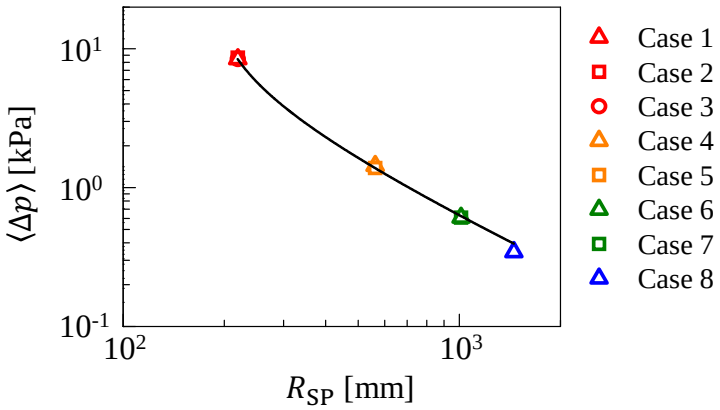

FIGURE 2.7: $\langle \Delta p \rangle$ of each case plotted against $R_{\rm SP}$. The solid line shows $\langle \Delta p \rangle = 830/(R_{\rm SP}\sqrt{\ln(R_{\rm SP}/179)})$ [kPa].

2.3.2 Peak-overpressure fluctuations

Statistical analyses are conducted for the fluctuation of Δp defined as $\Delta p' = \Delta p - \langle \Delta p \rangle$. Figure 2.8 shows the probability density functions (pdfs) of $\Delta p'$ normalized by

$\Delta p'_{\mathrm{rms}} = \langle \Delta p'^2 \rangle^{1/2}$. The Gaussian profile is also shown in Fig. 2.8, which seems to be in good agreement with the experimental results. To quantitatively evaluate the Gaussianity of the pdfs in Fig. 2.8, the skewness $\langle \Delta p'^3 \rangle / \Delta p'^3_{\mathrm{rms}}$ and flatness $\langle \Delta p'^4 \rangle / \Delta p'^4_{\mathrm{rms}}$ are plotted against $M_{\mathrm{T}}^2/(M_{\mathrm{S0}}^2 - 1)$ in Fig. 2.9. The skewness and flatness of $\Delta p'$ range from 0 to 0.4 and from 2.8 to 3.5, respectively, which are close to the values of the Gaussian profile (0 for skewness and 3 for flatness). Thus, the pdf of $\Delta p'$ is close to the Gaussian profile for $O(10^{-6}) \leq M_{\mathrm{T}}^2/(M_{\mathrm{S0}}^2 - 1) \leq O(10^{-2})$. Numerical simulations (Lee, Lele, and Moin, 1993; Larsson and Lele, 2009; Larsson, Bermejo-Moreno, and Lele, 2013) have investigated the density jump $\Delta\rho$ across the shock wave, where a linear relation can be found between $\Delta p'$ and the density jump fluctuation $\Delta\rho'$ as $\Delta p'/\langle \Delta p \rangle = m\Delta\rho'/\langle \Delta\rho \rangle$ (Eq. (A.5)). In numerical simulations by Larsson, Bermejo-Moreno, and Lele, 2013, the pdfs of $\Delta\rho$ are slightly skewed at higher M_{T} for $O(10^{-2}) \leq M_{\mathrm{T}}^2/(M_{\mathrm{S0}}^2 - 1) \leq O(10^{-1})$. However, the skewness of $\Delta\rho$ at $M_{\mathrm{T}}^2/(M_{\mathrm{S0}}^2 - 1) = 0.018$ and 0.11 estimated from their pdfs of $\Delta\rho$ are about 0.44 and 0.65, respectively, which are also not far from the Gaussian value.

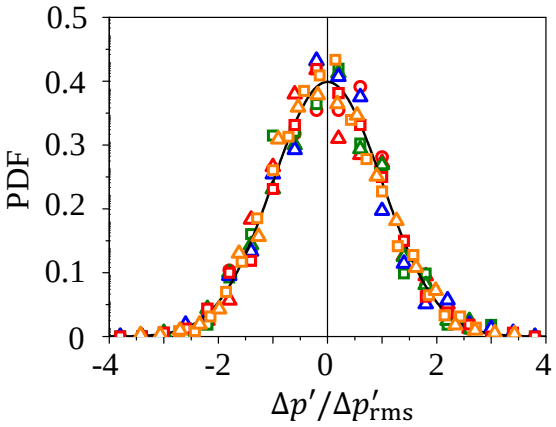

FIGURE 2.8: Pdfs of $\Delta p'/\Delta p'_{\mathrm{rms}}$ of each case. Symbols are common to Fig. 2.7. Black solid line shows the Gaussian profile.

In experiments of shock waves, there exist the peak-overpressure fluctuations that

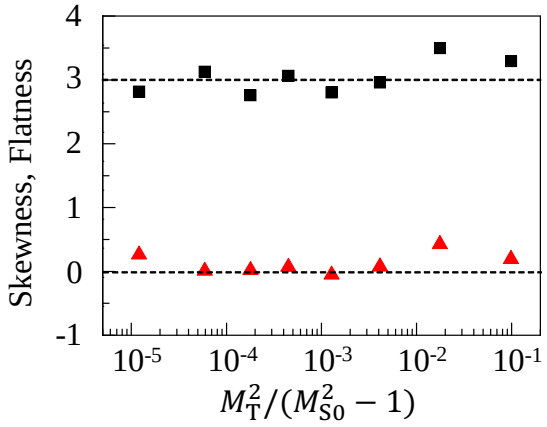

FIGURE 2.9: Skewness (triangle) and flatness (square) of $\Delta p'$ as a function of $M_T^2/(M_{S0}^2-1)$.

are inherently caused by an experimental facility. In our study, these can be evaluated by the experiments of the shock wave ejected in the flow without the grid, where the rms value of $\Delta p'$ is denoted by $(\Delta p'_{w/o})_{rms}$. Following Sasoh et al., 2014, the peak-overpressure fluctuations caused by turbulence are evaluated as $\sigma_{\Delta p} = [\Delta p'^2_{rms} - (\Delta p'_{w/o})^2_{rms}]^{1/2}$.

Figures 2.10(a) and (b) show $\sigma_{\Delta p}/\langle \Delta p \rangle$ plotted against $M_T/(M_{S0}-1)$ and $M_T^2/(M_{S0}^2-1)$, respectively. Figure 2.10 includes the experimental results of Sasoh et al., 2014 for M_{S0} = 1.0009 and low $M_T = O(10^{-4}\text{-}10^{-3})$. It also includes results of numerical simulations in two papers, which investigated a planar shock wave propagating in homogeneous isotropic turbulence with low $M_T = O(10^{-4})$ (Tanaka et al., 2018) and with high $M_T = 0.15$ or 0.37 (Larsson, Bermejo-Moreno, and Lele, 2013). M_{S0} is 1.1, 1.3, or 1.5 in Tanaka et al., 2018 while it is 1.5 in Larsson, Bermejo-Moreno, and Lele, 2013. Here, $\sigma_{\Delta p}/\langle \Delta p \rangle$ in Larsson, Bermejo-Moreno, and Lele, 2013 is obtained from Eq. (A.6) with density statistics calculated from the pdfs of the density jump across the shock wave presented in their paper. For fixed M_{S0} (M_{S0} = 1.0009 in Sasoh et al., 2014 and M_{S0} = 1.002, 1.004, and 1.021 in the present study), $\sigma_{\Delta p}/\langle \Delta p \rangle$

tends to increase with M_T. However, the results with different M_{S0} follow a different line in Fig. 2.10(a). On the other hand, $\sigma_{\Delta p}/\langle\Delta p\rangle$ plotted against $M_T^2/(M_{S0}^2-1)$ tends to collapse onto a single line in the logarithmic plot in Fig. 2.10(b), where $\sigma_{\Delta p}/\langle\Delta p\rangle$ obeys a power law of $M_T^2/(M_{S0}^2-1)$. The least square method applied to the data points in Fig. 2.10(b) yields $\sigma_{\Delta p}/\langle\Delta p\rangle = 0.669[M_T^2/(M_{S0}^2-1)]^{0.489}$ as shown in Fig. 2.10(b). The spherical shock waves used in Fig. 2.10 have different curvature radii R_{SP} depending on the experiments. In the present experiments, R_{SP} ranges between 219 mm and 1453 mm while R_{SP} = 215 [mm] is constant in Sasoh et al., 2014. Some of the experiments in the present study and in Sasoh et al. are conducted for similar values of $M_T^2/(M_{S0}^2-1)$ but with different R_{SP}. Comparison among these experiments shows that the relation between $\sigma_{\Delta p}/\langle\Delta p\rangle$ and $M_T^2/(M_{S0}^2-1)$ is not affected by R_{SP}.

2.4 Shock deformation model of turbulence effects on shock wave

2.4.1 Shock wave deformation by non-uniform velocity profile

The overpressure fluctuations behind a shock wave interacting with turbulence are studied with a shock deformation model, which considers a planar shock wave deformed by a local velocity fluctuation. In this model, the effects of turbulence on a shock wave are explained with the shock wave deformation due to non-uniformity of the velocity field. The model assumes that the velocity gradient in the tangential

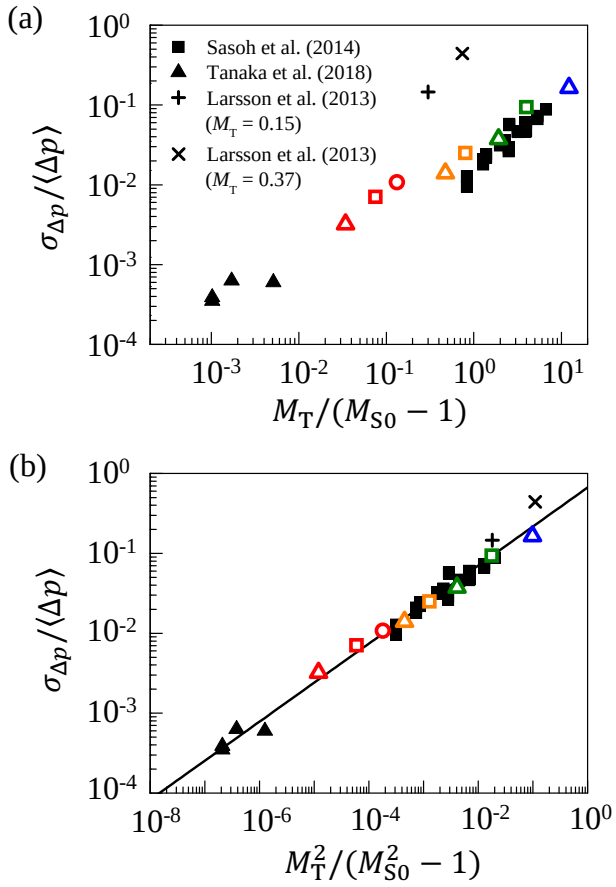

FIGURE 2.10: $\sigma_{\Delta p}/\langle\Delta p\rangle$ plotted against (a) $M_T/(M_{S0}-1)$ and (b) $M_T^2/(M_{S0}^2-1)$. Present experimental results are shown by symbols with color, which are common to Fig. 2.7. $\sigma_{\Delta p}/\langle\Delta p\rangle$ obtained by Sasoh et al., 2014 and Tanaka et al., 2018 are also plotted in the figures. $\sigma_{\Delta p}/\langle\Delta p\rangle$ estimated from the results by Larsson, Bermejo-Moreno, and Lele, 2013 are also shown for comparison. The straight line in (b) shows the power law $\sigma_{\Delta p}/\langle\Delta p\rangle = 0.669[M_T^2/(M_{S0}^2-1)]^{0.489}$ obtained by using the least squared method for $\sigma_{\Delta p}/\langle\Delta p\rangle$.

direction to the shock wave surface plays an important role in the shock deformation. The importance of the velocity gradient in the tangential direction was also confirmed in the recent numerical simulations, where strong correlation between the pressure gradient across the shock wave in the local shock normal direction and the velocity gradient of turbulence was reported (Tanaka et al., 2018). Therefore, the effects of turbulence are studied with the simplified model with the velocity profile that is non-uniform in the shock tangential direction. The model is used to estimate

the overpressure fluctuation level induced by the deformation.

The velocity fluctuation in the model is given by an axisymmetric velocity profile $u_{\mathrm{M}}(x,r)$, where x and r are the axial and radial coordinates. Temporal evolution of velocity fluctuations is not taken into account because of the small velocity fluctuation $u_{\mathrm{rms}} \ll U_{\mathrm{S0}}$ as in the present experiments, where the time scale of the turbulence is much larger than that of the shock wave propagation. A simple profile of u_{M} is considered in the model:

$$u_{\mathrm{M}}(x,r) = \begin{cases} u & (0 \le r \le r_0 \text{ and } 0 \le x \le x_l) \\ 0 & \text{otherwise} \end{cases}, \tag{2.11}$$

which has a constant velocity u in the cylindrical region defined with r_0 and x_l. The model considers influences of turbulence, where a large part of turbulent kinetic energy is contained in large-scale turbulent motions. Therefore, the distribution of u_{M} is related to large-scale motions. Thus, both r_0 and x_l are comparable with an integral length scale, where anisotropy of large scales is assumed to be weak as in the case of grid turbulence.

The model considers the planar shock wave propagating into the velocity field $u_{\mathrm{M}}(x,r)$ in x direction as illustrated in Fig. 2.11(a). The velocity of the shock wave movement is given by the sum of the shock propagation velocity $U_{\mathrm{S0}} = a_0 M_{\mathrm{S0}}$ and the fluid velocity on the shock wave. The shock movement velocity is U_{S0} for $r > r_0$ and $U_{\mathrm{S0}} + u$ for $r \le r_0$. Therefore, once the planar shock wave begins to propagate in the region with the velocity fluctuation u, the velocity of the shock wave movement becomes non-uniform and the shock wave begins to be deformed. However, since

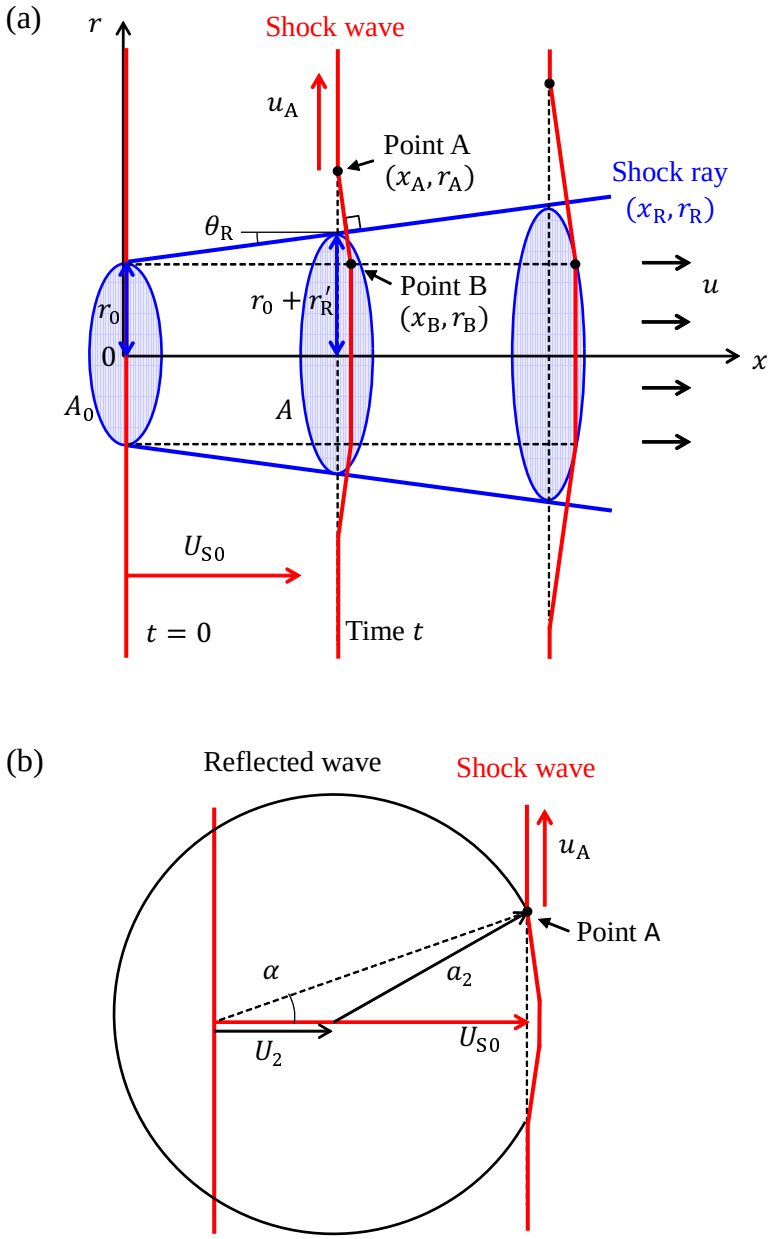

FIGURE 2.11: (a) Shock wave deformation due to a local velocity fluctuation u and (b) reflected wave propagation on the shock wave surface.

the shock wave surface needs to be connected at $r = r_0$, the inclination of the surface occurs from $r = r_0$. Therefore, the shock ray at $r = r_0$ also begins to be inclined as shown in Fig. 2.11(a), where the trajectories of the shock rays passing through $(x, r) = (0, r_0)$ are also shown with blue lines. The region surrounded by the infinite number of these shock rays is called a ray tube. In this model, the following

simplifications are considered for the calculation of the shock wave geometry:

- the deformation is so small ($x_A(t) \approx x_B(t)$) that $x_R(t) = x_A(t)$ is considered at time t for the calculation of r_R
- the shock wave surface area in the ray tube is equivalent to the cross sectional area of the ray tube at time t
- the inclination of the shock surface is linearly caused
- M_S is uniform in the cross section of the ray tube

The cross-sectional area A of the ray tube changes from $A = \pi r_0^2$ at $x = 0$ as the shock wave propagates. Once the trajectory of the shock ray (x_R, r_R) is determined, A at given $x = x_R$ can be computed as $A = \pi r_R^2$. The change in the area A results in the change in the shock Mach number M_S of the area (Whitham, 1957). The present model considers the turbulence effects on the shock Mach number through the change in A due to the velocity fluctuation u_M.

In the following discussion, the trajectories of the shock rays are obtained from the geometry of the shock wave because the shock ray is locally perpendicular to the shock wave surface. The change in M_S causes the pressure change behind the shock wave in the region of $r \leq r_0$. Then, a spherical reflected wave is formed because of the pressure change as shown in Fig. 2.11(b). For simplicity, the reflected wave is assumed to be isentropic, and the propagation of the reflected wave in the region of $r \leq r_0$ is not discussed below. The intersection of the non-deformed part of the shock wave and the reflected wave is shown as point A in Fig. 2.11(b). The reflected wave propagates with the characteristic velocity represented as the sum of the fluid velocity and sound speed behind the shock wave (Grasso and Pirozzoli, 2000). Figure 2.11(b)

shows the schematic of the reflected wave propagation on the shock wave surface, where a_2 and U_2 are the sound speed and fluid velocity behind the shock wave in the laboratory coordinate system, respectively. Here, U_2 and a_2 are assumed to be constant and independent from the change in M_S because $M'_S \equiv M_S - M_{S0} \ll M_{S0}$. The propagation velocity of the reflected wave in the r direction on the shock wave surface, u_A, is obtained from the geometrical relation of a_2, U_{S0}, and U_2:

$$u_A = \sqrt{a_2^2 - (U_{S0} - U_2)^2}, \tag{2.12}$$

which is also constant. The initial position of point A is $(x_A, r_A) = (0, r_0)$. Therefore. the trajectory of point A (x_A, r_A) is given by

$$x_A(t) = U_{S0} t, \tag{2.13}$$

$$r_A(t) = u_A t + r_0. \tag{2.14}$$

According to the Rankine-Hugoniot relations,

$$U_2 = \frac{2a_0}{\gamma+1}\left(M_{S0} - \frac{1}{M_{S0}}\right), \tag{2.15}$$

and

$$a_2 = a_0 \frac{\sqrt{(2\gamma M_{S0}^2 - \gamma + 1)\{(\gamma-1)M_{S0}^2 + 2\}}}{(\gamma+1)M_{S0}}. \tag{2.16}$$

In Fig. 2.11(b), α denotes the angle between the trajectory of point A and x axis in the laboratory coordinate system. From Eqs. (2.12), (2.15), and (2.16), $\tan\alpha = u_A/U_{S0}$

is written as a function of M_{S0}:

$$\tan\alpha = \frac{1}{M_{S0}^2}\sqrt{\frac{\{(\gamma-1)M_{S0}^2+2\}(M_{S0}^2-1)}{\gamma+1}}. \tag{2.17}$$

As the shock wave propagates, point A also propagates in r direction at speed u_A, and the inclined region of the shock wave expands. The phenomenon of the expansion of the inclined region caused by the reflected wave was also confirmed by previous experimental study on shock wave reflections over wedges (Sasoh, Takayama, and Saito, 1992) and theoretical study on shock-vortex interactions (Clavin, 2013). In the present model, the shock wave surface in $r_0 \le r \le r_A$ is described by the line connecting points A and B in Fig. 2.11(a). The trajectory of point B is obtained from $(\mathrm{d}x_B/\mathrm{d}t, \mathrm{d}r_B/\mathrm{d}t) = (U_{S0} + a_0 M_S' + u, 0)$, where the change in the Mach number due to the interaction with the velocity fluctuation is taken into account as $a_0 M_S'$:

$$x_B(t) = (U_{S0}+u)t + a_0\int_0^t M_S'(t^*)\mathrm{d}t^*, \tag{2.18}$$

$$r_B(t) = r_0. \tag{2.19}$$

Note that M_S' is assumed to be uniform in the cross section of the ray tube for simplicity. Because the shock ray is perpendicular to the line AB, the trajectory of the shock ray (x_R, r_R) can be determined as

$$\tan\theta_R \equiv \frac{\mathrm{d}r_R}{\mathrm{d}x_R} = \frac{x_B - x_A}{r_A - r_B}. \tag{2.20}$$

Substituting Eqs. (2.13), (2.14), (2.18), and (2.19) into Eq. (2.20) yields

$$\tan\theta_{\mathrm{R}} = \frac{ut + a_0 \int_0^t M_{\mathrm{S}}'(t^*)\mathrm{d}t^*}{u_{\mathrm{A}} t}. \tag{2.21}$$

With the trapezoidal rule, the integration in the numerator in Eq. (2.21) can simply be estimated as $\int_0^t M_{\mathrm{S}}'(t^*)\mathrm{d}t^* \approx M_{\mathrm{S}}' t/2$ with the initial condition $M_{\mathrm{S}}' = 0$ at $t = 0$:

$$\tan\theta_{\mathrm{R}} \approx \frac{u + a_0 M_{\mathrm{S}}'/2}{u_{\mathrm{A}}}. \tag{2.22}$$

For the ray tube whose radius is r_0 at $x_{\mathrm{R}} = 0$, its radius r_{R} at any time t can be calculated with Eq. (2.22). Then, the radius deviation $r_{\mathrm{R}}' = r_{\mathrm{R}} - r_0$ is

$$r_{\mathrm{R}}' = \int_0^{x_{\mathrm{R}}} \tan\theta_{\mathrm{R}} \mathrm{d}x_{\mathrm{R}}^* \approx \int_0^{x_{\mathrm{R}}} \frac{u + a_0 M_{\mathrm{S}}'/2}{u_{\mathrm{A}}} \mathrm{d}x_{\mathrm{R}}^*. \tag{2.23}$$

The deviation of $A = \pi r_{\mathrm{R}}^2$ from $A_0 = \pi r_0^2$, $A' = A - A_0$ can be written as

$$A' \approx 2\pi r_0 r_{\mathrm{R}}' \approx 2\pi r_0 \int_0^{x_{\mathrm{R}}} \frac{u + a_0 M_{\mathrm{S}}'/2}{u_{\mathrm{A}}} \mathrm{d}x_{\mathrm{R}}^*, \tag{2.24}$$

where small deformation $A' \ll A_0$ is assumed in the model. Equation (2.24) gives the fluctuation of the ray tube area as a function of $x_{\mathrm{R}}(t)$, which increases with time as the shock wave propagates. A'/A_0 can be written as

$$\frac{A'}{A_0} \approx \frac{2\pi r_0 r_{\mathrm{R}}'}{\pi r_0^2} \approx 2 \int_0^{x_{\mathrm{R}}} \frac{u + a_0 M_{\mathrm{S}}'/2}{U_{\mathrm{S0}} \tan\alpha} \frac{\mathrm{d}x_{\mathrm{R}}^*}{r_0} \equiv 2\xi, \tag{2.25}$$

where ξ is defined as $\xi \equiv A'/2A_0$.

2.4.2 Shock Mach number fluctuation for a weak shock wave

Hereafter, a weak shock wave is considered in the model as the present experiments are conducted for weak shock waves. The analysis for a strong shock wave is presented in Appendix B. The shock Mach number M_S of the ray tube with the area A is obtained from the relation (Whitham, 1957)

$$\frac{A}{A_0} = \exp\left(-\int_{M_{S0}}^{M_S} g(M_S^*)\mathrm{d}M_S^*\right), \tag{2.26}$$

where M_S^* is an integration variable. Here,

$$g(M_S) \equiv \frac{M_S}{M_S^2-1}\left(2\mu+1+\frac{1}{M_S^2}\right)\left(1+\frac{2}{\gamma+1}\frac{1-\mu^2}{\mu}\right) \tag{2.27}$$

and

$$\mu^2 \equiv \frac{(\gamma-1)M_S^2+2}{2\gamma M_S^2-\gamma+1}, \tag{2.28}$$

where γ is the heat capacity ratio. For a weak shock wave ($M_{S0} \to 1$), Eq. (2.26) can be simplified (Whitham, 1959) as

$$\frac{A}{A_0} \approx \left(\frac{M_{S0}-1}{M_S-1}\right)^2. \tag{2.29}$$

For $M_{S0} \lesssim 1.1$, the error of the A–M_S relation calculated with Eq. (2.29) from that calculated with Eq. (2.26) is within 10%. From Eqs. (2.25) and (2.29), the following relation is obtained for the shock Mach number of the deformed shock wave:

$$\left(\frac{M_{S0}-1}{M_S-1}\right)^2 - 1 \approx 2\xi, \tag{2.30}$$

which can be rewritten as

$$M'_{\mathrm{S}} \approx \frac{(\sqrt{2\xi+1}-1)(1-M_{\mathrm{S0}})}{\sqrt{2\xi+1}} \approx \xi(1-M_{\mathrm{S0}}), \tag{2.31}$$

where $\sqrt{2\xi+1} \approx \xi+1$ is used because $A' \ll A_0$. Differentiating both sides of Eq. (2.31) with respect to x_{R} gives the following differential equation:

$$\frac{\mathrm{d}M'_{\mathrm{S}}}{\mathrm{d}x_{\mathrm{R}}} \approx \frac{1-M_{\mathrm{S0}}}{r_0}\frac{u+a_0M'_{\mathrm{S}}/2}{U_{\mathrm{S0}}\tan\alpha}. \tag{2.32}$$

The solution of Eq. (2.32) is

$$M'_{\mathrm{S}} \approx -\frac{2u}{a_0}\left[1-\exp\left(-\frac{M_{\mathrm{S0}}-1}{2M_{\mathrm{S0}}\tan\alpha}\frac{x_{\mathrm{R}}}{r_0}\right)\right], \tag{2.33}$$

which yields M'_{S} as a function of x_{R}. Since the model assumes $x_l/r_0 \approx 1$, $M'_{\mathrm{S}l} \equiv M'_{\mathrm{S}}(x_l)$ is written as

$$M'_{\mathrm{S}l} \approx -\frac{2u}{a_0}\left[1-\exp\left(-\frac{M_{\mathrm{S0}}-1}{2M_{\mathrm{S0}}\tan\alpha}\right)\right]. \tag{2.34}$$

Here, $M'_{\mathrm{S}l}$ is M'_{S} caused when the shock wave propagates along the distance x_l. For $M_{\mathrm{S0}} \to 1$, $\exp\left(-\frac{M_{\mathrm{S0}}-1}{2M_{\mathrm{S0}}\tan\alpha}\right) \approx 1-\frac{M_{\mathrm{S0}}-1}{2M_{\mathrm{S0}}\tan\alpha}$, and Eq. (2.34) can be simplified as

$$M'_{\mathrm{S}l} \approx -\frac{u}{a_0}\frac{M_{\mathrm{S0}}-1}{M_{\mathrm{S0}}\tan\alpha}. \tag{2.35}$$

According to the Rankine-Hugoniot relations, Δp at $x_{\mathrm{R}} = x_l$ is

$$\Delta p = \frac{2\gamma p_0}{\gamma+1}\left[(M_{\mathrm{S0}}+M'_{\mathrm{S}l})^2-1\right], \tag{2.36}$$

where p_0 is the mean pressure in front of the shock wave. The ensemble average of Eq. (2.36) is

$$\langle \Delta p \rangle = \frac{2\gamma p_0}{\gamma+1}(M_{S0}^2 + \langle M_{Sl}'^2 \rangle - 1), \tag{2.37}$$

where $M_{S0} = \langle M_S \rangle$. For $M_{Sl}' \ll M_{S0}$, Eq. (2.37) gives

$$\langle \Delta p \rangle \approx \frac{2\gamma p_0}{\gamma+1}(M_{S0}^2 - 1). \tag{2.38}$$

On the other hand, the overpressure fluctuation $\Delta p' = \Delta p - \langle \Delta p \rangle$ is

$$\Delta p' = \frac{2\gamma p_0}{\gamma+1}(2M_{S0}M_{Sl}' + M_{Sl}'^2 - \langle M_{Sl}'^2 \rangle). \tag{2.39}$$

The terms of the second order of M_{Sl}' can be ignored in Eq. (2.39). Therefore, the following expression can be obtained:

$$\Delta p' \approx \frac{4\gamma}{\gamma+1} p_0 M_{S0} M_{Sl}'. \tag{2.40}$$

Equations (2.35), (2.38), and (2.40) yield the following relation between $\Delta p'$ and the velocity fluctuation:

$$\frac{\Delta p'}{\langle \Delta p \rangle} \approx \frac{2M_{S0}}{M_{S0}^2 - 1} M_{Sl}' \approx -\frac{u/a_0}{\tan\alpha}, \tag{2.41}$$

where $M_{S0} + 1 \approx 2$ for $M_{S0} \to 1$ is used. Here, $\tan\alpha$ given by Eq. (2.17) is simply represented as a function of the initial shock Mach number M_{S0}.

When the pdf of u follows the Gaussian profile as in many canonical turbulent flows (Pope, 2001), the linear relation between $\Delta p'$ and u in Eq. (2.41) shows that the pdf of $\Delta p'$ also follows the Gaussian profile. This implication from the model agrees

with the Gaussian pdf of the peak-overpressure fluctuations observed in Fig. 2.8 because grid turbulence has Gaussian velocity fluctuations. The standard deviations of both sides of Eq. (2.41) yield the relation among the rms peak-overpressure fluctuation, mean peak overpressure, shock Mach number, and turbulent Mach number:

$$\frac{\sigma_{\Delta p}}{\langle \Delta p \rangle} \approx \frac{1}{\sqrt{3}} \left(\frac{M_{\mathrm{T}}^2}{M_{\mathrm{S0}}^2 - 1} \right)^{1/2}, \tag{2.42}$$

where $\tan\alpha \approx \sqrt{M_{\mathrm{S0}}^2 - 1}$ is used because the weak shock wave has $M_{\mathrm{S0}} \to 1$. Hence, $\sigma_{\Delta p}/\langle \Delta p \rangle$ can be represented as a simple function of $M_{\mathrm{T}}^2/(M_{\mathrm{S0}}^2 - 1)$. This relation is well supported by the experimental results of the weak shock waves shown in Fig. 2.10(b), where the fitting to the power law $\sigma_{\Delta p}/\langle \Delta p \rangle = b_0[M_{\mathrm{T}}^2/(M_{\mathrm{S0}}^2 - 1)]^{b_1}$ yields $b_0 = 0.669$ and $b_1 = 0.489$, both of which agree well with Eq. (2.42). The present model obtains Eq. (2.42) from the deformation of the shock wave and the relation between the ray tube area and shock Mach number. Previous studies (Lee, Lele, and Moin, 1993; Larsson and Lele, 2009) also reported that $M_{\mathrm{T}}^2/(M_{\mathrm{S0}}^2 - 1)$ is an important parameter in the fluctuations of the shock wave dilatation or broken shock wave conditions. This parameter was considered as the ratio of the turbulent pressure fluctuations $\rho_0 u_{\mathrm{rms}}^2$ (ρ_0 is the density in front of the shock wave) to Δp. The present model implies that the shock Mach number fluctuation caused by the shock wave deformation is also important in the broken shock wave and the dilatation fluctuation.

2.4.3 Inclination angle of a shock wave

In classical studies, Ribner constructed a model for the shock inclination caused by a periodic velocity perturbation (Ribner, 1954; Ribner, 1955). In this section, we

compare the shock inclination angle obtained in our model with that obtained in Ribner's model. Since the shock wave surface is perpendicular to the shock ray, the inclination angle of the shock wave surface is equivalent to that of the shock ray. From Eqs. (2.22) and (2.35), the present model yields the inclination angle:

$$\frac{\tan\theta_{\mathrm{R}}}{u/a_0} \approx \frac{1}{M_{\mathrm{S}0}\tan\alpha}\left[1-\frac{M_{\mathrm{S}0}-1}{2M_{\mathrm{S}0}\tan\alpha}\right]. \tag{2.43}$$

On the other hand, Ribner assumed the shock inclination angle to be a sinusoidal function (Ribner, 1954) whose amplitude and wave number were determined by the sinusoidal velocity perturbation given in front of the shock wave, relation of the velocity across the shock wave, and linear perturbation theory. Hereafter, θ_{R} obtained in his study is denoted by θ_{RA}. θ_{RA} can be written as $\theta_{\mathrm{RA}} = \theta_{\mathrm{RA}0}\sin ky$, where $\theta_{\mathrm{RA}0}$ is the amplitude, k is the wave number, and y is the coordinate in the tangential direction of the shock wave surface. $\tan\theta_{\mathrm{RA}0}$ can be written as

$$\frac{\tan\theta_{\mathrm{RA}0}}{u/a_0} \approx \frac{1}{M_{\mathrm{S}0}}\frac{4\sqrt{1-\left(\frac{U_{\mathrm{S}0}-U_2}{a_2}\right)^2}\frac{U_{\mathrm{S}0}}{U_{\mathrm{S}0}-U_2}}{(\gamma+1)\left(\frac{U_{\mathrm{S}0}}{U_{\mathrm{S}0}-U_2}-1\right)} = 2M_{\mathrm{S}0}\sqrt{\frac{\gamma+1}{(2\gamma M_{\mathrm{S}0}^2-\gamma+1)(M_{\mathrm{S}0}^2-1)}}, \tag{2.44}$$

where $U_{\mathrm{S}0}-U_2$ is the velocity behind the shock wave in the shock fixed coordinate system, and $\theta_{\mathrm{RA}0} \approx \tan\theta_{\mathrm{RA}0}$ is used because of $\theta_{\mathrm{RA}0} \ll 1$. Figure 2.12 compares Eq. (2.43) with Eq. (2.44). While both are decrease functions of $M_{\mathrm{S}0}$, Eq. (2.44) is almost twice as large as Eq. (2.43) in $M_{\mathrm{S}0} \leq 1.5$. This is because $\tan\theta_{\mathrm{R}}/(u/a_0) \to 1/\sqrt{M_{\mathrm{S}0}^2-1}$ when $M_{\mathrm{S}0} \to 1$ while $\tan\theta_{\mathrm{RA}0}/(u/a_0) \to 2/\sqrt{M_{\mathrm{S}0}^2-1}$ when $M_{\mathrm{S}0} \to 1$. It is interesting that in both approaches, the inclination angle can be proportional to u/a_0 and $1/\sqrt{M_{\mathrm{S}0}^2-1}$ for $M_{\mathrm{S}0} \to 1$. With Eq. (2.44), however, A' becomes twice as

large as that obtained with Eq. (2.24), resulting in a twice value of $\sigma_{\Delta p}/\langle\Delta p\rangle$ than that obtained with Eq. (2.42) because of the linear relation among θ_{R}, A' and $\Delta p'$ described by Eqs. (2.25), (2.31), and (2.40).

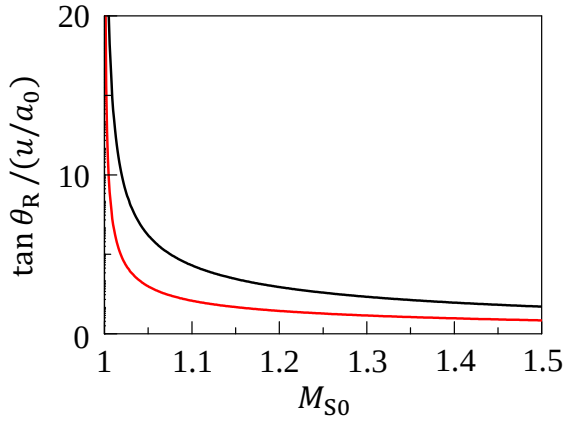

FIGURE 2.12: $\tan\theta_{\mathrm{R}}/(u/a_0)$ plotted against M_{S0}. Red and black lines are $\tan\theta_{\mathrm{R}}/(u/a_0)$ obtained with Eq. (2.43) and $\tan\theta_{\mathrm{RA0}}/(u/a_0)$ obtained with Eq. (2.44), respectively.

2.4.4 Condition for broken shock wave

The broken region of the shock wave surface is considered in the shock deformation model for the weak shock wave. The broken shock wave does not have a distinct jump in physical quantities at some parts of the shock wave surface, and the overpressure Δp in the broken region is much smaller than the average value $\langle\Delta p\rangle$. Here, the present thesis uses the term "broken region" to represent a local region without the jump on the shock wave surface while "broken shock wave" denotes the shock wave where the broken regions occupy an important fraction of the area on the shock wave surface. The broken region is detected as $\Delta\rho \leq \alpha_{\rho\mathrm{B}}\langle\Delta\rho\rangle$. $\alpha_{\rho\mathrm{B}}$ is chosen based on the results of numerical simulations of interactions between a planar shock wave and turbulence by Larsson, Bermejo-Moreno, and Lele, 2013, where the statistics of the density jump, $\Delta\rho$, across the shock wave were studied in detail. Because of Eq. (A.5),

$\Delta\rho \leq \alpha_{\rho\mathrm{B}}\langle\Delta\rho\rangle$ is equivalent to $\Delta p \leq \alpha_{p\mathrm{B}}\langle\Delta p\rangle$, where $\alpha_{p\mathrm{B}} \equiv m(\alpha_{\rho\mathrm{B}}-1)+1$. Their simulations with $M_\mathrm{T}=0.37$ and $M_{\mathrm{S}0}=1.5$, which is considered as the broken shock wave case, show that the broken region is well detected by $\alpha_{\rho\mathrm{B}}$ between 0.1 and 0.6 ($\alpha_{p\mathrm{B}}$ between 0.017 and 0.56). For $\alpha_{\rho\mathrm{B}}=0.1$ and 0.6 ($\alpha_{p\mathrm{B}}=0.017$ and 0.56), the detected broken regions occupy 0.05 % and 10 % on the shock wave surface, respectively.

A cumulative distribution function of $\Delta p/\langle\Delta p\rangle$, $F(\alpha)$, that represents a probability of events with $\Delta p/\langle\Delta p\rangle \leq \alpha$, can be obtained by integrating the pdf of $\Delta p/\langle\Delta p\rangle$ from 0 to α. Since the broken region is defined as $\Delta p/\langle\Delta p\rangle \leq \alpha_{p\mathrm{B}}$, $F(\alpha=\alpha_{p\mathrm{B}})$ yields the fraction of the broken regions on the shock wave surface. F can be computed from the pdf of $\Delta p'/\langle\Delta p\rangle$. The pdf of u is assumed to follow the Gaussian profile as in grid turbulence:

$$\mathrm{PDF}(u) = \frac{1}{\sqrt{2\pi}}\exp\left(-\frac{u^2}{2u_\mathrm{rms}^2}\right). \tag{2.45}$$

In this case, the pdf of $\Delta p'/\langle\Delta p\rangle$ in the shock deformation model is also expressed by the Gaussian profile because of the linear relation between u and $\Delta p'$ in Eq. (2.41). The pdf of $\Delta p'/\langle\Delta p\rangle$ is obtained as a function of $M_\mathrm{T}^2/(M_{\mathrm{S}0}^2-1)$ because the variance of $\Delta p'/\langle\Delta p\rangle$ is written as Eq. (2.42). Therefore, $F(\alpha)$ in the shock deformation model depends on the parameter $M_\mathrm{T}^2/(M_{\mathrm{S}0}^2-1)$. The fraction of the broken regions $F(\alpha_{p\mathrm{B}};M_\mathrm{T}^2/(M_{\mathrm{S}0}^2-1))$ is numerically computed for $\alpha_{p\mathrm{B}}=0.017$ and 0.56 in $10^{-2} \leq M_\mathrm{T}^2/(M_{\mathrm{S}0}^2-1) \leq 10^0$. Figure 2.13 shows F as a function of $M_\mathrm{T}^2/(M_{\mathrm{S}0}^2-1)$. When $M_\mathrm{T}^2/(M_{\mathrm{S}0}^2-1)$ is of order of 10^{-1}, the fraction of the broken regions for $0.017 \leq \alpha_{p\mathrm{B}} \leq 0.56$ rapidly increases, and F for $\alpha_{p\mathrm{B}}=0.017$ and $\alpha_{p\mathrm{B}}=0.56$

exceed 0.05 % and 10 %, respectively. Therefore, the broken shock wave is expected to appear for $M_T^2/(M_{S0}^2-1) \geq O(10^{-1})$. This condition is consistent with the numerical results, (Lee, Lele, and Moin, 1993; Larsson and Lele, 2009; Larsson, Bermejo-Moreno, and Lele, 2013) where the broken shock wave was also found for $M_T^2/(M_{S0}^2-1) \geq O(10^{-1})$. It is important to note that these numerical simulations consider compressible turbulence at much higher turbulent Mach number than in the present experiments. The model does not consider temperature and density fluctuations, which can exist in front of the shock wave propagating through compressible turbulence. Therefore, the model might not be accurate for the shock/turbulence interaction with high turbulent Mach number.

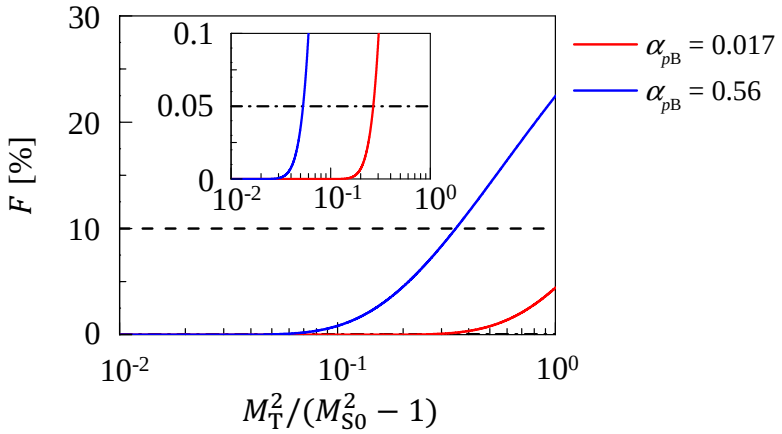

FIGURE 2.13: Cumulative distribution function $F(\alpha_{pB})$, which represents the probability of $\Delta p/\langle \Delta p \rangle \leq \alpha_{pB}$ for α_{pB} = 0.017 (red) and 0.56 (blue), plotted against $M_T^2/(M_{S0}^2-1)$. Horizontal dashed-dotted line and broken line show F = 0.05 [%] and 10 [%], respectively.

Compressible turbulence at high turbulent Mach number causes fluctuations in density and temperature as well as fluid properties such as a viscosity coefficient, and the influences of compressible turbulence on the shock wave are much more complicated than those of incompressible turbulence. It should be noted that in Fig. 2.10(b), $\sigma_{\Delta\rho}/\langle \Delta\rho \rangle$ at $M_T = 0.37$ by Larsson, Bermejo-Moreno, and Lele, 2013

shows a greater deviation from the fitting line than at $M_T = 0.15$, indicating that the compressibility of turbulence can affect the fluctuations in the density or pressure jump across a shock wave. Therefore, in the case with compressible turbulence, the broken shock wave can be caused even at smaller $M_T^2/(M_{S0}^2 - 1)$ than in the case with incompressible turbulence, though the broken shock criterion can be $M_T^2/(M_{S0}^2 - 1) \geq O(10^{-1})$ in both cases.

2.5 Summary of this chapter

The wind tunnel experiments on a weak spherical shock wave propagating in grid turbulence at a low turbulent Mach number have been conducted, and the statistics of peak-overpressure fluctuations for various values of $M_T^2/(M_{S0}^2 - 1)$ have been investigated. The rms peak-overpressure fluctuation normalized by the averaged peak overpressure, $\sigma_{\Delta p}/\langle \Delta p \rangle$, is shown to follow a power law of $M_T^2/(M_{S0}^2 - 1)$. Fitting of experimental results in present and previous studies indicates $\sigma_{\Delta p}/\langle \Delta p \rangle = 0.669[M_T^2/(M_{S0}^2 - 1)]^{0.489}$. The pdfs of the peak-overpressure fluctuations are very close to the Gaussian profile for a wide range of $M_T^2/(M_{S0}^2 - 1)$ from $O(10^{-6})$ to $O(10^{-2})$.

The shock deformation model has been proposed for the influences of turbulence on the shock wave. The model relates the shock Mach number fluctuation induced by turbulence to the shock wave deformation due to the non-uniform velocity fluctuation, where the change in the cross-sectional area of the ray tube caused by the deformation produces the shock Mach number fluctuation. The model for a weak shock wave yields the relation $\sigma_{\Delta p}/\langle \Delta p \rangle \approx (1/\sqrt{3})[M_T^2/(M_{S0}^2 - 1)]^{1/2}$, which is consistent

with the experimental results. The Gaussianity of the peak-overpressure fluctuations is also obtained from the model when the velocity fluctuations are Gaussian, which is also consistent with the present experiments. The model also predicts that the broken shock wave appears in the case of $M_{\mathrm{T}}^2/(M_{\mathrm{S0}}^2 - 1) \geq O(10^{-1})$.

Chapter 3

Finite response time of shock wave modulation by turbulence

3.1 Introduction of this chapter

As addressed in the previous chapters, one of the interesting problems in shock-turbulence interactions is the modulation of a shock wave, which has been observed as a post-shock wave overpressure fluctuation induced by turbulence (Lipkens and Blackstock, 1998a; Dokukina et al., 2013; Sasoh et al., 2014; Kim, Sasoh, and Matsuda, 2010). It has been found that the level of the post-shock overpressure fluctuation depends on the turbulence intensity. However, in most previous experiments on shock-turbulence interaction, since the characteristics of turbulence and shock wave were not obtained simultaneously, the relation remains unclear between the turbulence and the shock wave modulation. Detailed investigations require simultaneous and quantitative measurements of shock wave and turbulence, which is characterized by spatiotemporal fluctuations with a wide range of scales of motions. In this

study, the experiments on shock-turbulence interaction are conducted in a wind tunnel, where the velocity of turbulence and the overpressure behind a shock wave which interacts with turbulence are simultaneously measured.

3.2 Experimental methods

The effects of grid turbulence on the overpressure behind a spherical shock wave are investigated with wind tunnel experiments. Figure 3.1 describes the experimental setup. Here, the experiments are conducted with the same facility as in Chapter

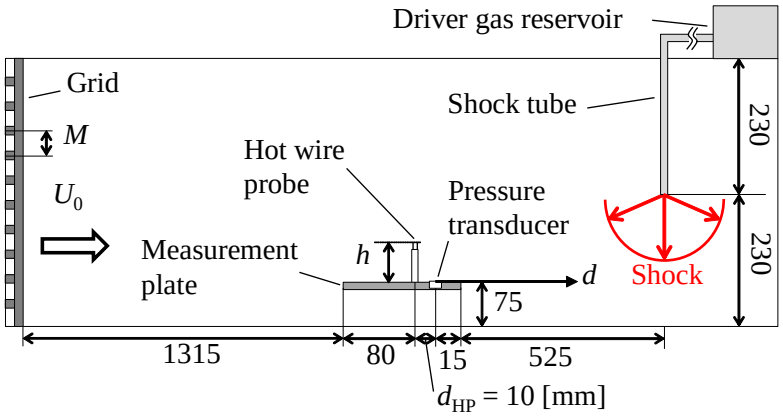

FIGURE 3.1: Side view of experimental setup. Lengths are shown in mm.

2, and brief explanations are given below. Between the grid and the open end of the shock tube, a measurement plate with the thickness of 5 mm is installed, on which a piezoelectric pressure transducer (PCB Piezotronics Inc. 113B27) and an I-type hot-wire probe (DANTEC DYNAMICS 55P11) are mounted (see Fig. 3.1) for the measurements of overpressure P on the plate and streamwise velocity U. This plate is also used in Chapter 2. However, in the experiments in this Chapter, the plate is equipped with both a pressure transducer and a hot-wire probe for the

simultaneous measurements. The shock Mach number is set to $M_{S0} = 1.004$ on the measurement plate by adjusting the distance between the open end of the shock tube and the pressure transducer location. The experimental conditions are summarized in Tab. 3.1, which also includes turbulence characteristics at the velocity measurement location. The Kolmogorov microscale η is calculated as $\eta = (\nu^3/\varepsilon)^{1/4}$, where the energy dissipation rate ε is obtained by using the relation for isotropic turbulence, $\varepsilon = 15\nu u_{\mathrm{rms}}^2/\lambda^2$ (Nieuwstadt, Westerweel, and Boersma, 2016). With the shock wave generator and the measurement system controlled by a computer, the sampling of the signals of P and U with the oscilloscope (YOKOGAWA DL 750) at a sampling rate 1 MHz is started 50 ms before the shock wave is ejected from the open end. The velocity measurement height h defined in Fig. 3.1 is ranged from 15 mm to 125 mm. As explained below, the velocity signal recorded before the shock wave ejection is used for estimating streamwise profiles of velocity at the instance of the shock ejection. In each measurement condition, 500 runs of the shock wave were used for the statistical analysis. Note that the statistics with 300 runs yield qualitatively the same results discussed below.

3.3 Analysis on relation between velocity and overpressure fluctuations

The relation between the peak-overpressure fluctuation and the velocity fluctuation is analyzed for the evaluation of the effects of the instantaneous turbulent velocity profile on the overpressure fluctuation. Here, the post-process of the velocity signal for

TABLE 3.1: Experimental conditions of grid turbulence and the rms peak-overpressure fluctuation $\Delta p'_{\mathrm{rms}}$ induced by grid turbulence. The table also includes the mesh Reynolds numbered Re_M, the rms streamwise velocity fluctuation u_{rms}, Kolmogorov microscale η, Taylor microscale λ, and longitudinal integral length scale L_u, at the measurement location.

Case	M50-U10	M50-U20	M100-U10	M100-U20
Symbol	△	◯	▽	□
M [mm]	50	50	100	100
U_0 [m/s]	10	20	10	20
Re_M	3.35×10^4	6.7×10^4	6.7×10^4	13.4×10^4
η [mm]	0.198	0.134	0.163	0.112
λ [mm]	3.92	3.75	3.91	3.78
L_u [mm]	27.5	48.1	54.3	64.3
u_{rms} [m/s]	0.387	0.798	0.568	1.17
$\Delta p'_{\mathrm{rms}}/\langle \Delta p \rangle$	0.0269	0.0620	0.0338	0.0703

the calculation of the velocity fluctuation and the analysis of the correlation between the overpressure and velocity fluctuations are described.

Figure 3.2(a) shows an example of simultaneous measurements of P and U plotted against time t_{c}, where $t_{\mathrm{c}} = 0$ is the time when the peak-overpressure Δp is measured at the pressure transducer. The change in P with the shock wave is discussed in Chapter 2. As well as the change in P, the rapid decrease in U and gradual increase after the decrease can also be caused by the shock wave arrival and by the expansion wave that follows the shock wave, respectively. Hereafter, the streamwise distance measured from the pressure transducer is denoted by d. The positive direction of d is shown in Fig. 3.1, which is the same as that of U. Since the eddy-turnover time of the turbulence $L_u/u_{\mathrm{rms}} \sim 10^2$ [ms] is much larger than the shock propagation time from the shock-tube end to the pressure transducer $L/U_{\mathrm{S0}} \sim 10^0$ [ms], the turbulence velocity signal U can be assumed to be frozen in the streamwise direction during the shock propagation. Hence, the Taylor's hypothesis can be used to convert

time series data $U(t_c)$ to the streamwise profile of $U(d)$ at the probe height. Since there is a streamwise distance d_{HP} (= 10 [mm]) between the pressure transducer and the hot wire, the convection distance of the velocity signal $U(t_c)$ from the pressure transducer location, d is calculated as

$$d = -U_0 t_c - d_{HP}. \tag{3.1}$$

d in Eq. (3.1) represents the streamwise location of the turbulence velocity signal U at the shock arrival time which is measured at the hot wire at time t_c. In Fig. 3.2(b), U is plotted against t_c and d. With Eq. (3.1), the turbulence velocity at d, $U(d)$ is calculated at the moment when the shock wave is ejected. The decay of grid-turbulence is not important in the range of d considered here (Kitamura et al., 2014). Since the time-averaged turbulence velocity U_{ave} is much smaller than the shock wave propagation velocity U_{S0}, the turbulence convection in the streamwise direction can be ignored while the shock wave is propagating. Thus, the shock wave propagates upstream through the turbulence whose velocity profile at h is represented by $U(d)$, and reaches the pressure transducer location.

Furthermore, as shown in Fig. 3.3, the low pass filtered velocity with a cutoff length Δd is calculated as

$$\overline{U}(d,\Delta d) = \frac{1}{\Delta d}\int_{-\Delta d/2}^{\Delta d/2} U(d+\delta)\mathrm{d}\delta, \tag{3.2}$$

which is the velocity of motions in scales larger than Δd at the location d. Thus, we are able to investigate the relation between the overpressure and the turbulent motions at the location d with the scales larger than Δd. Note that when $U(d)$ is

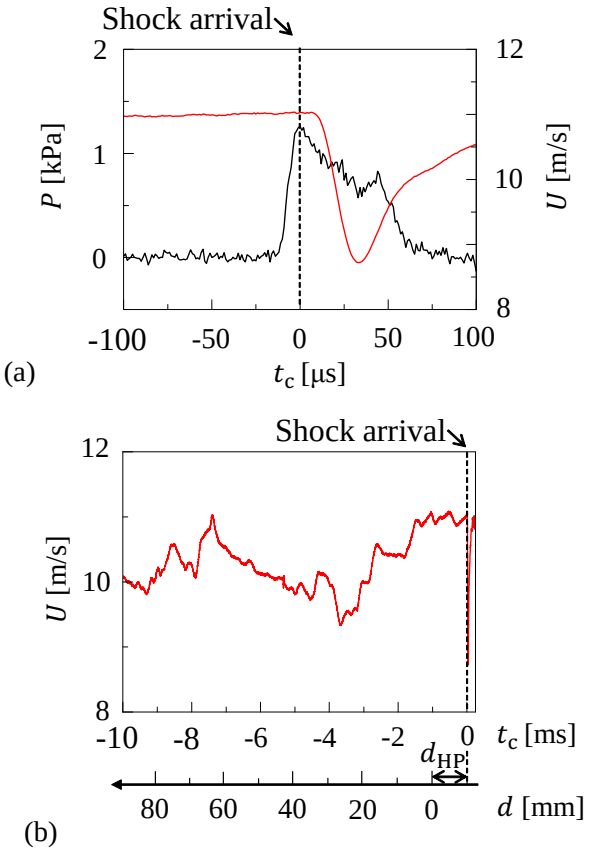

FIGURE 3.2: (a) Example of results of simultaneous measurements of overpressure P (black) and turbulence velocity U (red) plotted against t_c. (b) Velocity signal U in (a) plotted against t_c and d. Broken vertical line shows the shock arrival time.

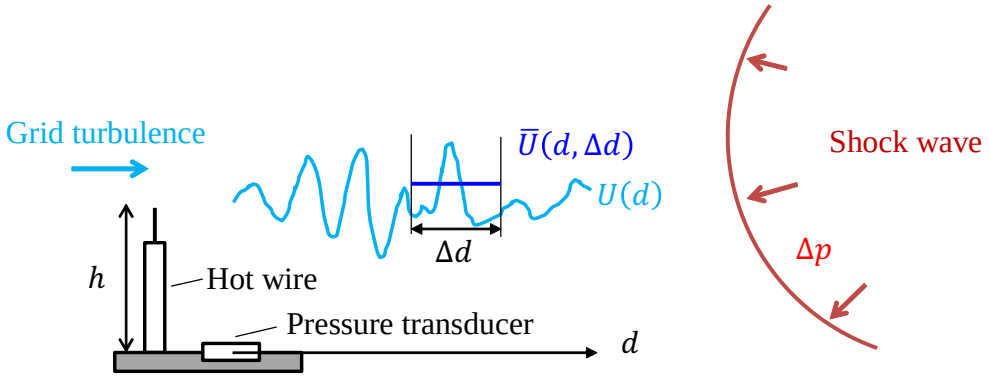

FIGURE 3.3: Schematic of the velocity analysis of $\overline{U}(d,\Delta d)$.

given for $0 \leq d \leq L$, the maximum value of Δd is restricted by d and L as

$$0 \leq \Delta d \leq \begin{cases} 2d & (0 \leq d \leq L/2) \\ 2(L-d) & (L/2 < d \leq L). \end{cases} \tag{3.3}$$

In the present experiments, $L = 540$ [mm]. The fluctuation of $\overline{U}$ from the time-averaged velocity U_{ave} is

$$\hat{u}(d,\Delta d) = \overline{U}(d,\Delta d) - U_{\mathrm{ave}}. \tag{3.4}$$

The relation between the peak overpressure fluctuation $\Delta p'$ and $\hat{u}(d,\Delta d)$ is investigated by calculating the correlation coefficient R between $\Delta p'$ and $\hat{u}(d,\Delta d)$ at the velocity measurement height h as

$$R(d,\Delta d) = \frac{\langle \hat{u}\Delta p' \rangle}{\sqrt{\langle \hat{u}^2 \rangle \langle \Delta p'^2 \rangle}}. \tag{3.5}$$

3.4 Results

Figures 3.4 (a)-(d) show examples of the scatter plots of $(\Delta p'/\langle \Delta p \rangle, \hat{u}/U_0)$ obtained at certain $(d,\Delta d,h)$ in each experimental condition. From each figure, the correlation coefficients can be calculated as $R = 0.294$, 0.280, 0.330, and 0.302. For the following discussions, R is calculated for all $(d,\Delta d)$ and h considered in the present experiments.

Figures 3.5-3.8 show $R(d,\Delta d)$ obtained at different h in all cases, where the velocity and peak-overpressure fluctuations are found to be positively correlated. This

means that the overpressure behind the shock wave increases when the fluctuating velocity vector is opposed to the direction of the shock propagation and vise versa. This is consistent with the experimental work on shock-jet interaction by Ribner, Morris, and Chu, 1973, where the shock wave strength was amplified when it interacted with the jet flowing in the opposite direction of the shock wave propagation. Similar profiles of $R(d,\Delta d)$ were also obtained for all cases. A high correlation can be observed for the velocity fluctuation at a specific location d and a scale Δd. A maximum value of R is denoted as $R_{\max}$. $(d_{\max},\Delta d_{\max})$ is the point of $(d,\Delta d)$ where $R_{\max}$ is obtained, which is shown with the crosses in Figs. 3.5-3.8. One can find a strong dependence of $d_{\max}$ on h while an h-dependence of $\Delta d_{\max}$ is not very clear. $\Delta d_{\max}$ is of the order of the integral scale, suggesting that turbulent motions which affect the peak overpressure are related to the large scales (see Tab. 3.1). Figure 3.9 plots $d_{\max}$ against h compared with the shock ray toward the pressure transducer location. The plots are mostly on the ray, which indicates that the peak overpressure is affected by the turbulence around the ray.

Figure 3.10 shows the relation between $d_{\max}$ and $R_{\max}$, both of which can be obtained as a function of h in each experimental condition. $R_{\max}$ decreases with $d_{\max}$ after it has reached the maximum, confirming that the turbulence very far away from the pressure transducer location has a small influence on the peak overpressure. Since the shock wave is continuously affected by turbulence during the propagation, the influences of turbulence on the shock wave modulation at earlier time of the propagation are somehow negated by turbulence near the pressure transducer location.

Interestingly, the strongest correlation is not related to the smallest $d_{\max}$ (the smallest h), but is observed at some distance away from the pressure transducer

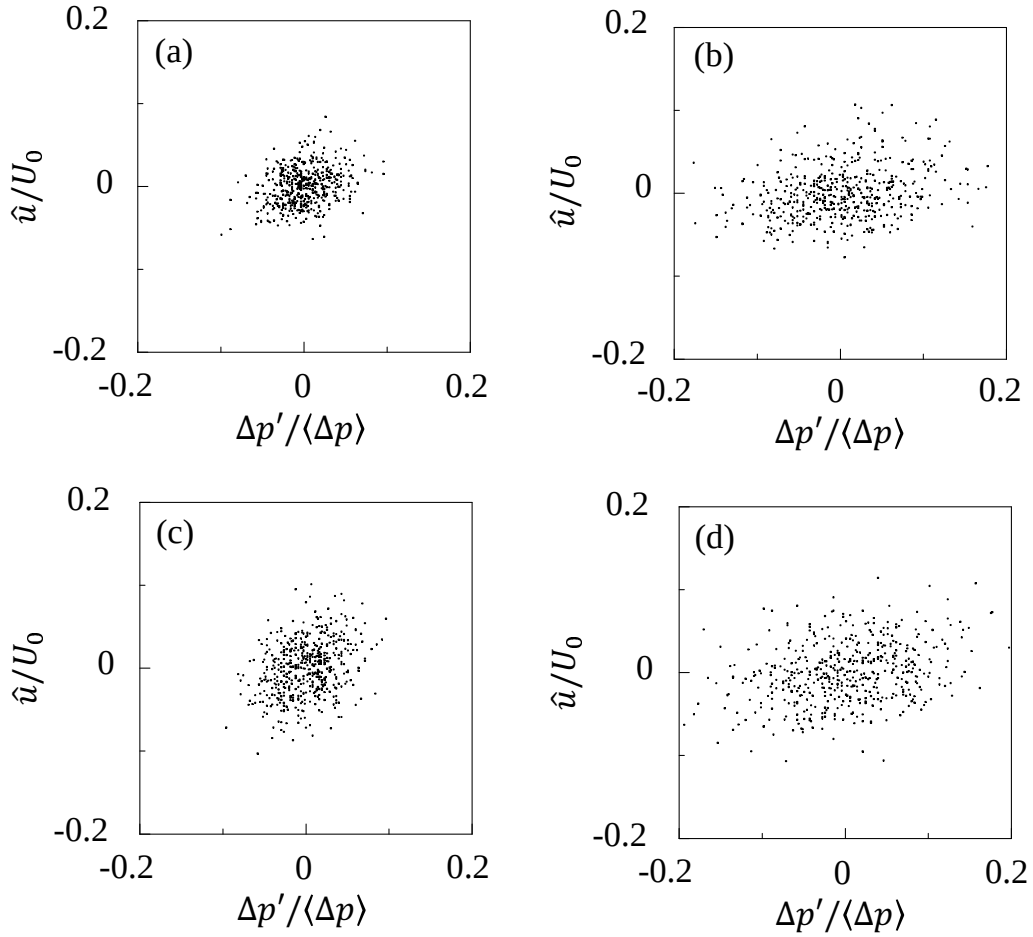

FIGURE 3.4: Scatter plots of $(\Delta p'/\langle \Delta p \rangle, \hat{u}/U_0)$ obtained for (a) M50-U10 at $(d, \Delta d, h) = (141, 120, 40)$ [mm], (b) M50-U20 at $(d, \Delta d, h) = (119, 119, 25)$ [mm], (c) M100-U10 at $(d, \Delta d, h) = (173, 162, 50)$ [mm], and (d) M100-U20 at $(d, \Delta d, h) = (222, 139, 50)$ [mm].

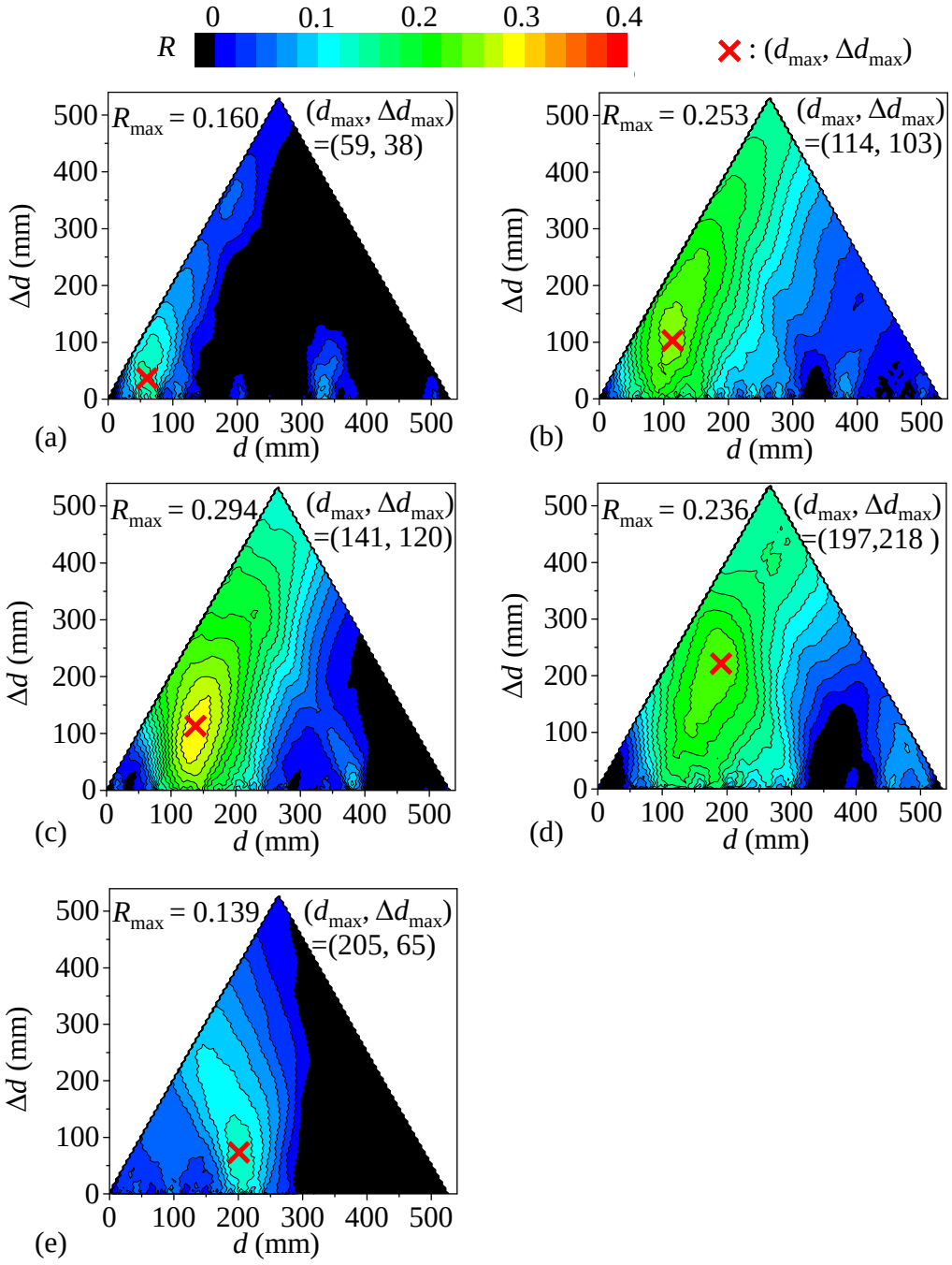

FIGURE 3.5: Correlation coefficients $R(d,\Delta d)$ between peak-overpressure fluctuation and velocity fluctuation for M50-U10 measured at h of (a) 15 mm, (b) 25 mm, (c) 40 mm, (d) 45 mm, and (e) 50 mm. The crosses show $(d,\Delta d) = (d_{\max},\Delta d_{\max})$, where R has a maximum value $R_{\max}$ in each figure.

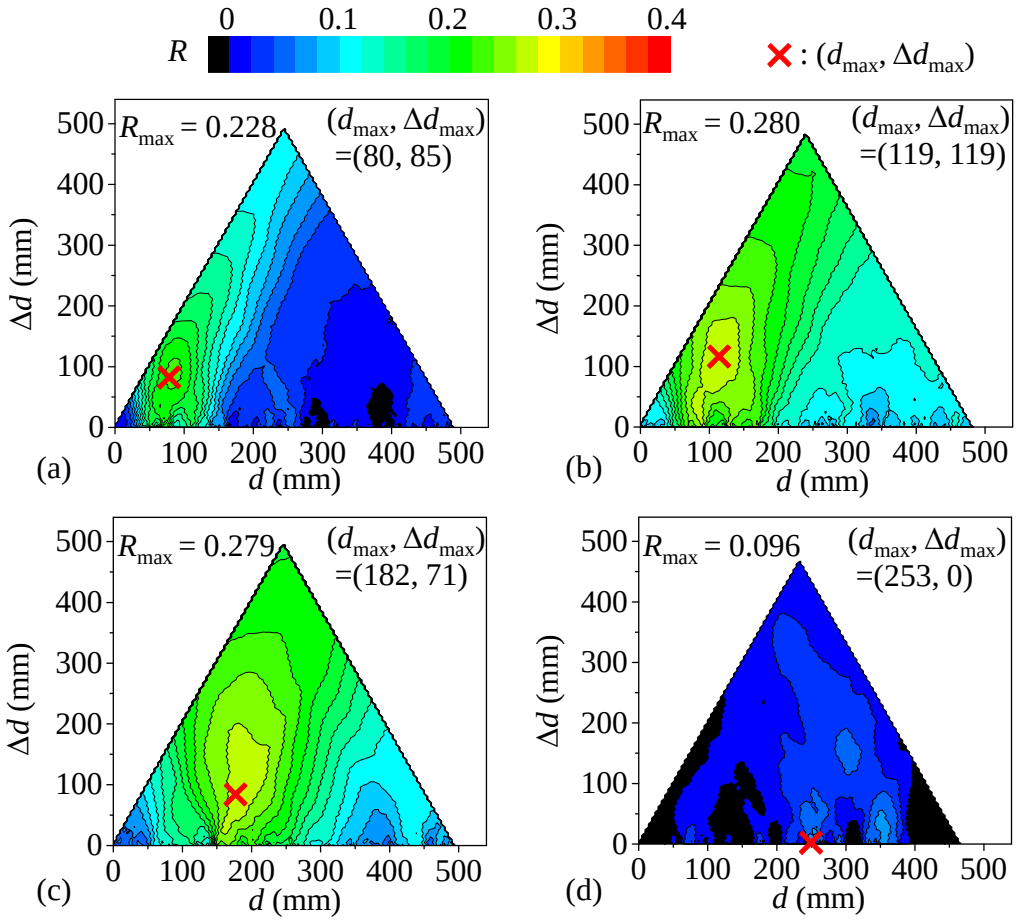

FIGURE 3.6: Correlation coefficients $R(d,\Delta d)$ between peak-overpressure fluctuation and velocity fluctuation for M50-U20 measured at h of (a) 15 mm, (b) 25 mm, (c) 50 mm, and (d) 75 mm. The crosses show $(d,\Delta d) = (d_{\max},\Delta d_{\max})$, where R has a maximum value $R_{\max}$ in each figure.

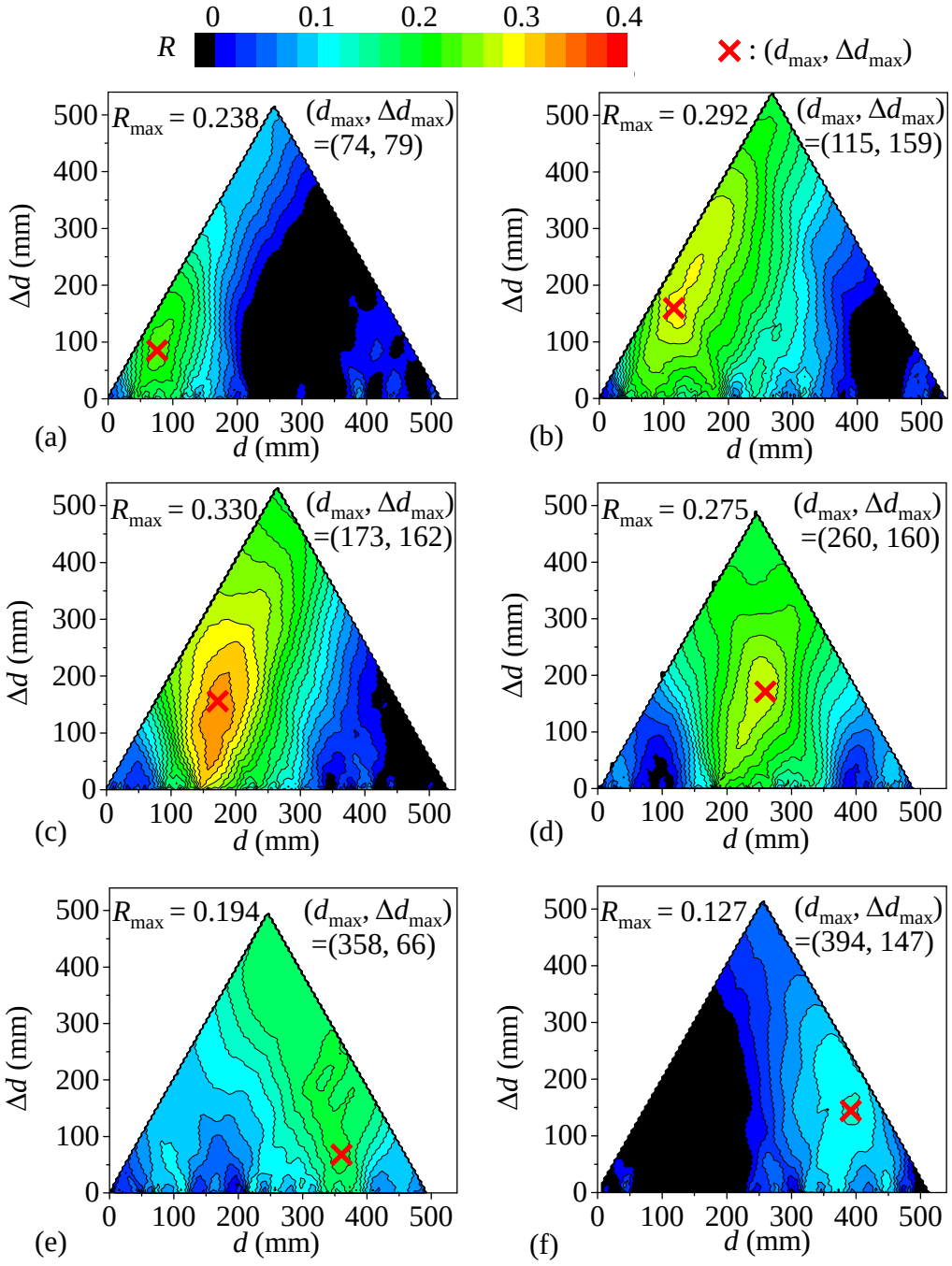

FIGURE 3.7: Correlation coefficients $R(d,\Delta d)$ between peak-overpressure fluctuation and velocity fluctuation for M100-U10 measured at h of (a) 15 mm, (b) 25 mm, (c) 50 mm, (d) 75 mm, (e) 100 mm, and (f) 125 mm. The crosses show $(d,\Delta d) = (d_{\max},\Delta d_{\max})$, where R has a maximum value $R_{\max}$ in each figure.

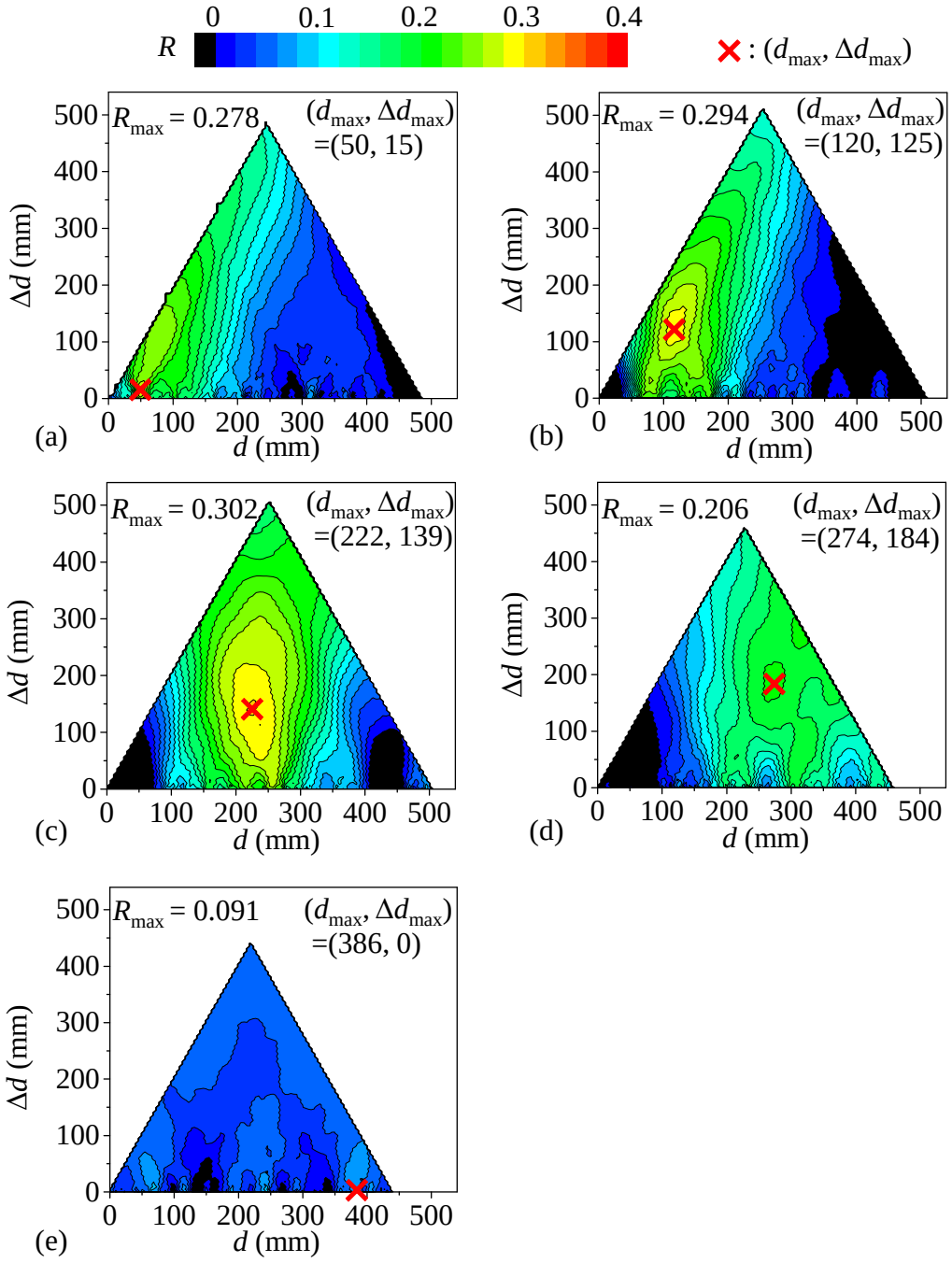

FIGURE 3.8: Correlation coefficients $R(d,\Delta d)$ between peak-overpressure fluctuation and velocity fluctuation for M100-U20 measured at h of (a) 15 mm, (b) 25 mm, (c) 50 mm, (d) 75 mm, and (e) 100 mm. The crosses show $(d,\Delta d) = (d_{\max},\Delta d_{\max})$, where R has a maximum value $R_{\max}$ in each figure.

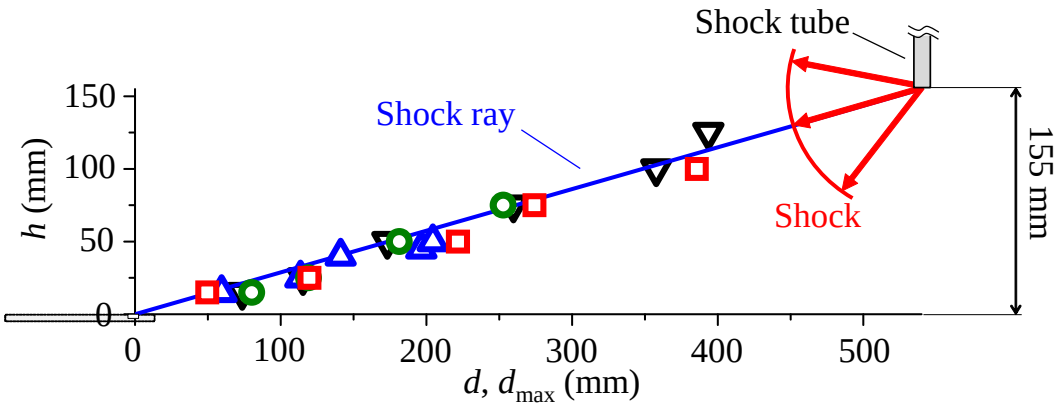

FIGURE 3.9: Relation between $d_{\max}$ and h. Blue line shows the shock ray along which the shock wave propagates toward the pressure transducer location ($d = 0$, $h = 0$). See Tab. 3.1 for symbols.

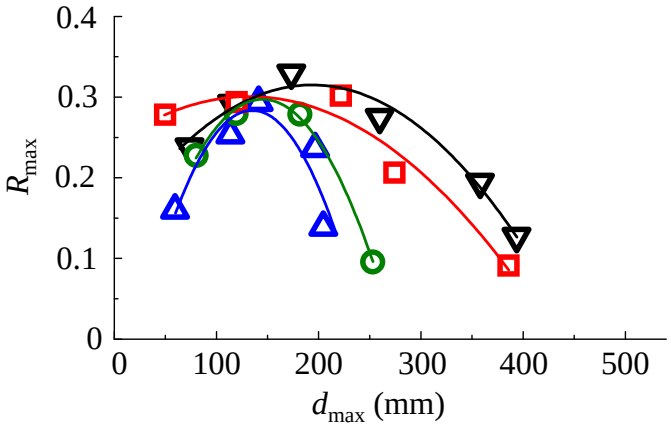

FIGURE 3.10: Relation between $d_{\max}$ and $R_{\max}$. Solid lines are quadratic approximations. See Tab. 3.1 for symbols.

TABLE 3.2: d_P/η, d_P/λ, d_P/L_u for each experimental case.

Case	M50-U10	M50-U20	M100-U10	M100-U20
d_P/η	682	1080	1190	1180
d_P/λ	34.5	38.7	49.6	35.0
d_P/L_u	4.91	3.01	3.57	2.05

location. A plausible interpretation of this result is that it takes a finite time for the post-shock wave overpressure to change after the shock wave is interfered with turbulence. The concept of the response time is consistent with numerical simulations of shock/vortex interactions by Grasso and Pirozzoli, 2000, where the shock wave deformation by the vortex is more significant slightly after the shock wave has passed the vortex than while the shock wave is propagating within the vortex (the deformation can cause the post-shock wave overpressure modulation; see Whitham, 1957). In order to investigate the response time, it is useful to introduce d_P defined as d_{max} corresponding to a maximum value of R_{max} in Fig. 3.10, where d_P is estimated with the quadratic fitting. d_P can be related to the time required for the turbulent effects on the overpressure to be the most significant. To compare the response distance d_P with the turbulence length scales, Tab. 3.2 shows d_P/η, d_P/λ, and d_P/Lu. Apparently, the response distance d_P in all cases is much larger than η and λ, and the integral length/time scale is an appropriate quantity of turbulence characterizing the response distance/time.

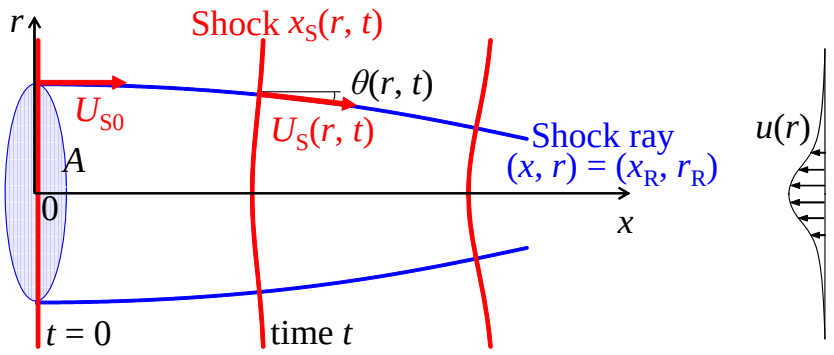

FIGURE 3.11: Shock wave deformation model by a local flow disturbance $u(r)$ with the shock wave surface location x_S (red) and shock ray trajectory (x_R, r_R) (blue).

3.5 A theoretical model for response time of shock modulation

The shock deformation model developed in Chapter 2 is used to study the response distance/time of the post-shock wave overpressure modulation by turbulence with a simple model of axisymmetric deformation of a shock wave by a local flow disturbance. Here, the discussion with the model is simplified from Chapter 2 as in this chapter, the model is used only for predicting a qualitative behavior of the shock wave propagating in a non-uniform velocity profile. The model assumes that a plane shock wave with the shock Mach number M_{S0} and the propagation velocity $U_{S0} = M_{S0}a_0$ at the initial state ($t = 0$) encounters the velocity fluctuation centered at $r = 0$ as in Fig. 3.11. A circle control area A embedded on the shock wave at $t = 0$ changes with the shock wave deformation. The perimeter of A is tracked along the shock ray with the shock propagation, whose direction is locally normal to the shock wave. A temporal variation of A is estimated by the velocity fluctuation $u(r)$ characterized

by u_{rms} and lateral integral length scale L_{ur}, which is related to the large-scale turbulent motions. Positive u denotes the velocity against the shock wave propagation direction. As considered in Chapter 2, the velocity gradient in r direction is important, and following discussion assumes $\partial u/\partial x = 0$. Generally, $u(r)$ is given as $u_{\mathrm{rms}} f(\tilde{r})$ ($\tilde{r} = r/L_{ur}$) with a dimensionless function f, where for positive u, $f(0) = 1$ and $f(r)$ monotonically decreases to 0 with r. Similarly, negative u is represented with $f(r)$ which monotonically increases from $f(0) = -1$ to 0 with r. The non-uniform shock wave motion by $u(r)$ causes the shock wave surface to be inclined, where an angle between the x axis and the shock ray is $\theta(r,t)$. The x-coordinate of the shock wave surface location, $x_{\mathrm{S}}(r,t)$, changes with the velocity of the shock wave motion $U_{\mathrm{S}} \cos\theta - u(r)$, where the propagation velocity of the deformed shock wave is $U_{\mathrm{S}}(r,t) = M_{\mathrm{S}}(r,t)a$. Note that $M_{\mathrm{S}}(r,t)$ is the shock Mach number of the deformed shock wave, and U_{S} is the velocity perpendicular to the deformed shock wave surface.

U_{S} can be represented by $U_{\mathrm{S}} = U_{\mathrm{S0}} + \delta U_{\mathrm{S}}$ with the perturbation δU_{S} induced by the shock wave deformation. δU_{S} is related to the modulated overpressure. When the change in the overpressure due to velocity disturbance is given by $\Delta p'_{\mathrm{rms}}$ listed in Tab. 3.1, δU_{S} estimated from the Rankine-Hugoniot relations is about $u_{\mathrm{rms}}/10^1$ ($\approx U_{\mathrm{S0}}/10^4$). Therefore, for simplicity, the shock wave movement velocity in the x direction is given by $U_{\mathrm{S}} \cos\theta - u(r) \approx U_{\mathrm{S0}} - u(r)$, where the weak deformation is considered ($\theta(r,t) \ll 1$), and the contribution for δU_{S} is ignored when compared with U_{S0}. We can derive the shock wave surface location $x_{\mathrm{S}}(r,t) = (U_{\mathrm{S0}} - u(r))t$,

where the initial location of the shock wave is $x_S(r,0) = 0$. Then, $\theta(r,t)$ is given by

$$\tan\theta(r,t) = \frac{\partial x_S}{\partial r} = -u'(r)t, \tag{3.6}$$

where $u'(r) = \mathrm{d}u/\mathrm{d}r$. The trajectory of the shock ray $(x_R(t), r_R(t))$ is orthogonal to the shock wave surface: $\mathrm{d}r_R/\mathrm{d}x_R = -\tan\theta(r_R,t)$. Since the shock wave surface satisfies Eq. (3.6), the trajectory is

$$\frac{\mathrm{d}r_R}{\mathrm{d}x_R} = u'(r_R)t = \frac{x_R u'(r_R)}{U_{S0} - u(r_R)}. \tag{3.7}$$

With the initial location $(x_R, r_R) = (0, r_0)$, $U_{S0} \gg u_{rms}$, and $u(r) = u_{rms} f(\tilde{r})$, Eq. (3.7) yields

$$\frac{x_R}{L_{ur}} \approx \sqrt{2\frac{U_{S0}}{u_{rms}} \int_{\tilde{r}_0}^{\tilde{r}_R} \frac{\mathrm{d}\tilde{r}^*}{f'(\tilde{r}^*)}}, \tag{3.8}$$

where $\tilde{r}_0 = r_0/L_{ur}$ and $\tilde{r}_R = r_R/L_{ur}$.

Since $\mathrm{d}M_S/\mathrm{d}A < 0$ ($\mathrm{d}M_S/\mathrm{d}r_R < 0$) (Whitham, 1957) and Δp across the shock wave increases with M_S, we have $\mathrm{d}(\Delta p)/\mathrm{d}r_R < 0$, which is consistent with previous studies of the relation between the shock wave overpressure modulation and its deformation (e.g., Kim, Sasoh, and Matsuda, 2010). When $U_{S0} \gg |u|$ as in our experiments, the sign of $\mathrm{d}r_R/\mathrm{d}x_R$, Eq. (3.7), is determined by u'. When $u > 0$, $u' < 0$ as in the case of Fig. 3.11, resulting in $\mathrm{d}r_R/\mathrm{d}x_R < 0$. Thus, as the shock wave propagates (x_R increases) in the turbulence with $u > 0$, r_R decreases, resulting in the increase in the overpressure and shock Mach number because of $\mathrm{d}M_S/\mathrm{d}r_R < 0$. In a similar way, $u < 0$ results in the decrease in M_S and Δp. Thus, the present model of the shock

wave modulation also predicts the positive correlation observed in Figs. 3.5-3.8.

Since $|\mathrm{d}r_\mathrm{R}/\mathrm{d}t|$ monotonically increases from $|\mathrm{d}r_\mathrm{R}/\mathrm{d}t| = 0$ at $t = 0$, the change in r_R and Δp at the earlier time is much slower than the later time. The change in Δp in the model becomes large after a certain period of time, which is called the response time in this thesis. During this time period, the shock wave propagates over a certain distance called the response distance. Thus, the model is also consistent with the experimental finding of the finite response time, which is confirmed with the high correlation away from the wall in Fig. 3.10.

In the following discussion, the response time and distance are denoted by t_p and x_p, respectively. Because x_p is given by $x_p = x_\mathrm{R}(t_p)$, where x_R follows Eq. (3.8) with $r_\mathrm{R}(t_p)$, the following scaling law can be derived for the response distance x_p:

$$\frac{x_p}{L_{ur}} \propto \left(\frac{u_\mathrm{rms}}{U_\mathrm{S0}}\right)^{-0.5} = \left(\frac{M_\mathrm{T}}{M_\mathrm{S0}}\right)^{-0.5}, \tag{3.9}$$

where $M_\mathrm{T} = u_\mathrm{rms}/a_0$ is the turbulent Mach number. It should be noticed that the shock wave deformation in the model is caused by the shear $\mathrm{d}u(r)/\mathrm{d}r$. The shear time scale for $u(r)$ is given by $t_e = L_{ur}/u_\mathrm{rms}$, which is also known as the large-eddy turnover time. Then, we have a scaling for the response time t_p, which is equivalent to Eq. (3.9):

$$\frac{t_p}{t_e} \propto \left(\frac{M_\mathrm{T}}{M_\mathrm{S0}}\right)^{0.5}. \tag{3.10}$$

In Fig. 3.12, the response distance estimated as d_P in the experiments is compared with Eq. (3.9), where d_P/L_u is plotted against $M_\mathrm{T}/M_\mathrm{S0}$ (L_u is used here since L_{ur} is proportional to L_u in the grid turbulence (Kitamura et al., 2014). d_P/L_u decreases

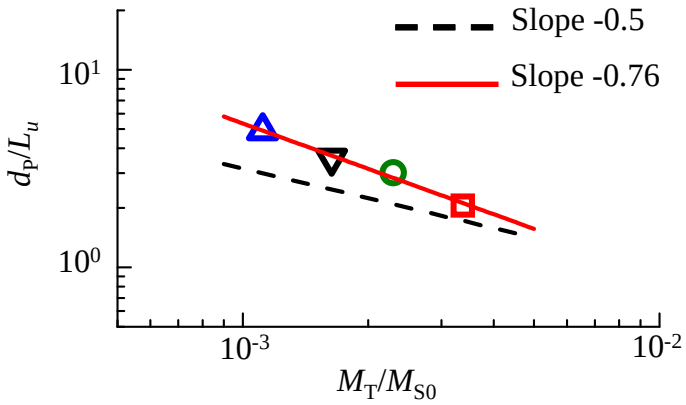

FIGURE 3.12: Relation between d_p/L_u and M_T/M_{S0}. Broken line shows Eq. (3.9). See Tab. 3.1 for symbols.

with M_T/M_{S0} with the power law $d_P/L_u \propto (M_T/M_{S0})^{-0.76}$, which is fairly close to the prediction in Eq. (3.9) obtained by a very simple model of the shock deformation due to a local flow disturbance.

3.6 Summary of this chapter

The experiments on interaction between a shock wave and grid turbulence in a wind tunnel have been conducted, and the overpressure behind the shock wave and the velocity of the grid turbulence have been measured simultaneously. The analysis on the correlation between the velocity and peak overpressure has confirmed finite response time of the post-shock wave overpressure modulation due to turbulence. The modulation is induced by the large-scale turbulent motions around the shock ray while the turbulence influences become significant in the overpressure behind the shock wave after it propagates over a certain distance (response distance). A simple model has been proposed for the modulation based on the small deformation of shock wave by a local flow disturbance, in which the response time is related to

the small-deformation timescale of the shock wave. The model well explains the correlation between the turbulence velocity fluctuation and the peak-overpressure fluctuation behind the shock wave. This model predicts that the response time is proportional to the product of the large-eddy turnover time and $(M_T/M_{S0})^{0.5}$ while the response distance is given as the product of the shock wave propagation velocity and the response time. It has been shown that the scaling for the response distance expected from the model is recovered fairly well in the experiments considering the simplicity of the model.

Chapter 4

Statistical properties of spherical shock waves propagating through grid turbulence, turbulent cylinder wake, and laminar flow

4.1 Introduction of this chapter

In most numerical studies, homogeneous isotropic turbulence has been considered for shock-turbulence interaction (Lee, Lele, and Moin, 1993; Larsson and Lele, 2009; Larsson, Bermejo-Moreno, and Lele, 2013; Ryu and Livescu, 2014; Chen and Donzis, 2019) since it does not have directivity, which is advantaged to simplify the shock-turbulence interaction phenomena. This is necessary for understanding the fundamental aspects of the phenomena. In experimental studies of shock-turbulence interaction, grid turbulence has been used as a model of quasi-isotropic turbulence

for shock-turbulence interaction studies (Keller and Merzkirch, 1994; Agui, Briassulis, and Andreopoulos, 2005; Tamba et al., 2016; Salze et al., 2014; Tamba et al., 2019). Chapters 2 and 3 in this thesis also considered grid turbulence for the evaluation of the effects of the velocity fluctuation of turbulence on the overpressure behind a shock wave. On the other hand, in the practical problems, turbulence is usually inhomogeneous. For example, in sonic boom problem caused by supersonic flight, the shock wave propagates in the atmospheric turbulence, whose statistical properties of atmospheric turbulence vary in space (Fujino et al., 2017). Inhomogeneous turbulence such as jet has also been used for shock-turbulence interaction study such as in Lipkens and Blackstock, 1998c and Kim, Sasoh, and Matsuda, 2010, however, these studies did not focus on the effects of inhomogeneity of turbulent characteristics on a shock wave, which remain unclear. In this study, the interaction between a spherical shock wave and turbulence is studied with grid turbulence, single-cylinder wake, and double-cylinder wake for investigating the influence of inhomogeneous turbulence on the shock wave characteristics.

4.2 Experimental methods

4.2.1 Experimental setup

The schematic of the experimental setup is shown in Fig. 4.1. The wind tunnel and the shock generator are the same as those used in the studies in Chapters 2 and 3. The streamwise, vertical, and spanwise directions are denoted by x, y, and z, respectively. The measurement system with a pressure transducer, an I-type hot wire, and

measurement plate is also same in the study in Chapter 3. The shock Mach number at the pressure transducer location is 1.004.

Turbulence is generated in the wind tunnel by a conventional grid or cylinder(s). The grid turbulence experiment uses the grid with $M = 100$ [mm], which is also used in Chapters 2 and 3. The pressure transducer location is 1405 mm downstream from the grid. The grid turbulence experiment at the same condition was studied in Chapter 3. In the cylinder wake experiments, on the other hand, the cylinders with a diameter of $D = 10$ [mm] are horizontally placed in the test section. The experiments of a single-cylinder wake and a double-cylinder wake interacting with the shock wave are conducted. In the former case, one cylinder is placed at $h = 75$ [mm] above the measurement plate. The streamwise distance between the hot-wire probe and the cylinder is 500 mm. In the latter case, in addition to the cylinder at $h = 75$ [mm], another cylinder is also placed at $h = 25$ [mm]. The cylinders at $h = 75$ [mm] and 25 [mm] are called 'reference cylinder' (RC) and 'disturbance cylinder' (DC), respectively. Figure 4.1 shows the experimental setup for the double-cylinder experiment. The distance between the DC and the hot wire probe is denoted by x_{DC}. In this configuration, the shock wave toward the measurement plate passes through the DC wake region after it interacts with the RC wake. The characteristics of the DC wake, which affects the shock wave, can be varied by changing x_{DC} since the turbulent wake develops in the streamwise direction. Thus, in the double-cylinder experiments, we can investigate the effects of the width of the turbulent region and nonuniformity of the turbulent intensity, varied by the installation of DC, on the change in the shock wave statistics. In addition to these experiments with turbulence, the experiments are also performed for a laminar flow without the grid nor cylinders.

Thus, four types of experiments: with grid turbulence, a single-cylinder wake, a double-cylinder wake, and a laminar flow, are conducted in the present study. The purpose of the present experiments is to investigate the following issues: (i) how the influence of turbulence (RC wake) on the shock wave is modified by another turbulence at a different location (DC wake); (ii) the influence of inhomogeneous and intermittent turbulence on the shock wave. (i) is mainly investigated with the single- and double-cylinder experiments while the experimental results with the grid turbulence and single- and double-cylinder wake(s) are compared for elucidating (ii).

The wind tunnel is operated at the streamwise mean velocity of U_0 = 10 [m/s]. The Reynolds number based on the cylinder diameter is $Re_D = U_0 D/\nu = 6.9 \times 10^3$. The mesh Reynolds number is $Re_M = U_0 M/\nu = 6.7 \times 10^4$ for the grid turbulence.

4.2.2 Velocity characteristics of cylinder wake

Prior to the experiments with the shock wave, statistics of streamwise velocity of the single-cylinder wake are examined with the I-type hot wire probe on the wake center-line, where the cylinder is installed at 230 mm above the floor of the test section. Figures 4.2 (a) and (b) show the mean velocity defect $\Delta U = U_0 - U_{\rm ave}$ and rms velocity fluctuation $u_{\rm rms}$ for the single-cylinder wake as a function of the streamwise distance ξ_1 from the cylinder center, respectively. Here, $U_{\rm ave}$ is obtained by time-averaging the instantaneous streamwise velocity U. From $\xi_1/D = 15$ to 125, ΔU divided by U_0 decays from 0.3 to 0.1. Turbulent intensity of a cylinder wake is known to decay following a power law (Osaka et al., 1983). The present results show that $u_{\rm rms}/U_0$ decays with $u_{\rm rms}/U_0 = 0.861(\xi_1/D + 6.51)^{-0.611}$. Figures 4.2 (c) and (d) show λ

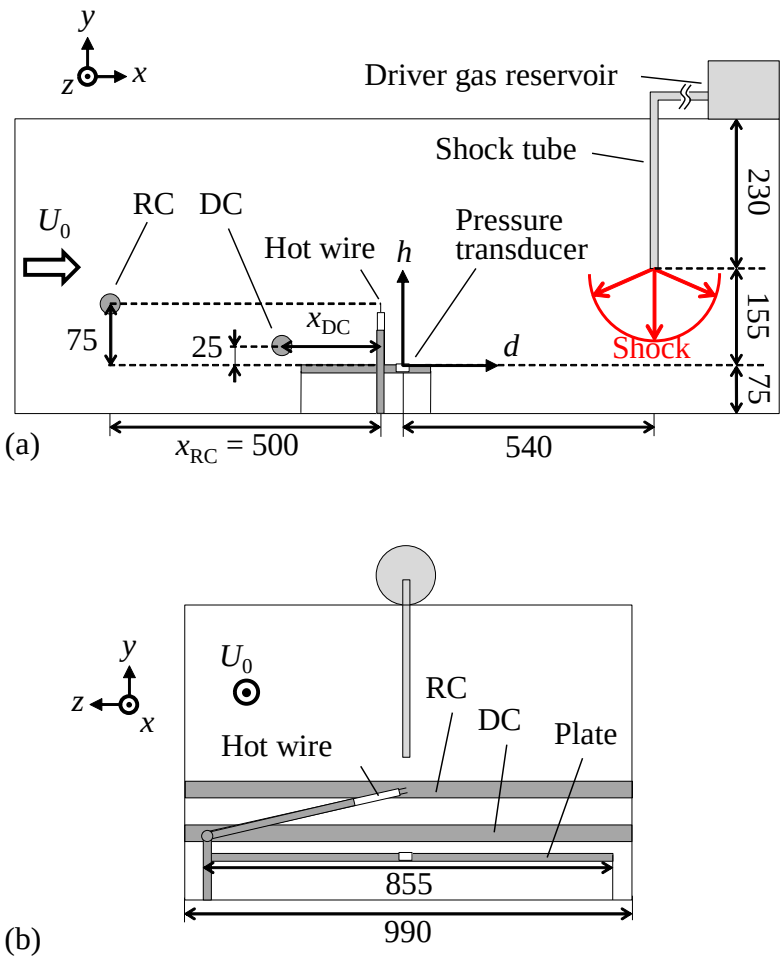

FIGURE 4.1: Schematic of test section seen from (a) spanwise direction and (b) streamwise direction. Lengths are shown in mm.

and L_u of ξ_1, respectively. The increase in these length scales in the streamwise direction with the power law of $(\xi_1/D + \xi_0/D)$ can be confirmed as in the previous study (Osaka et al., 1983). Here, ξ_0 is the virtual origin considered for the calculation of the fitting line. Least square method applied to the experimental results yields $\lambda^2/D^2 = 0.00297(\xi_1/D + 4.95)$ and $L_u/D = 1.10(\xi_1/D + 3.40)^{0.369}$. Figure 4.3 shows the energy spectra of frequency f of velocity fluctuations $u = U - U_{\mathrm{ave}}$ of the single-cylinder wake at 500 mm downstream of the cylinder, the grid turbulence at 1405 mm downstream of the grid, and the laminar flow. The energy spectra for the grid turbulence and cylinder wake show that the velocity fluctuations are distributed

in a wide frequency range, consistent with a typical energy spectrum in turbulence. We can also confirm that the energy spectrum for the grid turbulence follows Kolmogorov's $k^{-5/3}$ law.

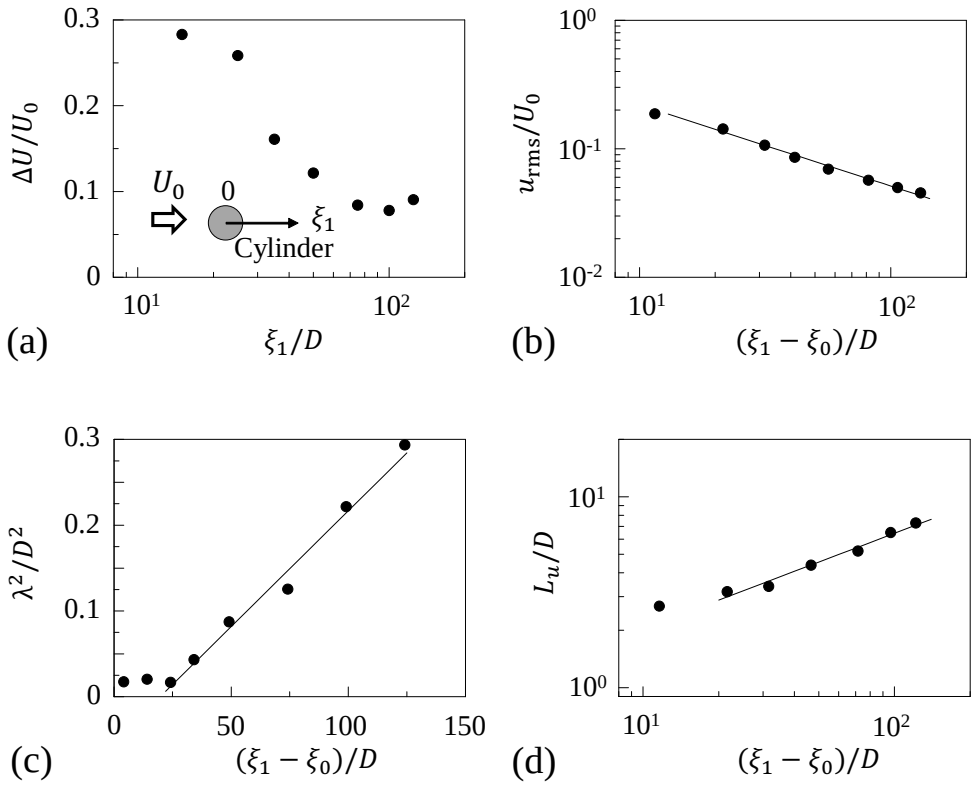

FIGURE 4.2: (a) $\Delta U/U_0$, (b) $u_{\rm rms}/U_0$, (c) λ^2/D^2, and (d) L_u/D as a function of the streamwise distance ξ_1 from the cylinder center. Solid lines in each figure show $u_{\rm rms}/U_0 = 0.861(\xi_1/D+6.51)^{-0.611}$, $\lambda^2/D^2 = 0.00297(\xi_1/D+4.95)$, and $L_u/D = 1.10(\xi_1/D+3.40)^{0.369}$, respectively.

4.2.3 Experimental conditions

The double-cylinder experiments are performed for three different streamwise locations of the DC: $x_{\rm DC} = 150$, 200, and 300 [mm], which correspond to $x_{\rm DC}/D = 15$, 20, and 30, respectively.

For shock-turbulence interaction experiments, U at $h = 75$ [mm] and the overpressure on the plate are simultaneously measured with the I-type hot wire probe and

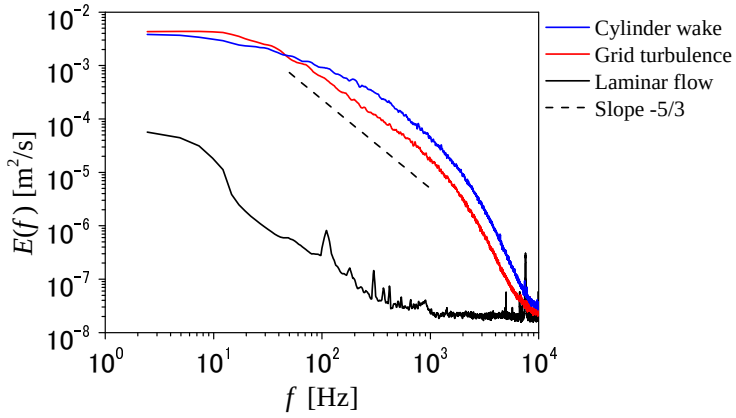

FIGURE 4.3: Energy spectra of velocity fluctuation u for the cylinder wake, grid turbulence, and laminar flow

the pressure transducer installed as shown in Fig. 4.1. This height, $h = 75$ [mm], is on the wake centerline of the RC in the experiments with cylinders. The hot wire probe is supported on the plate at a different spanwise location from the pressure transducer so that the probe does not disturb the turbulence on the x-y plane at the spanwise location of the measurements. The shock ejection and the signal sampling at 1 MHz with an oscilloscope (YOKOGAWA DL750) are controlled by a computer. Sampling is started before the shock wave ejection. The correlation between the peak overpressure and velocity is investigated with the same method as in Chapter 3. Here, the velocity is measured at $h = 75$ [mm] in all the experiments. Therefore, a peak in the overpressure upon the shock wave arrival is studied in relation to the velocity at $h = 75$ [mm]. The measurements are repeated for 500 runs of the shock wave ejections (50 runs for the laminar flow case) for the statistical analysis.

Table 4.1 shows the streamwise distance from the hot-wire probe to the grid, RC, and DC, denoted by x_{G}, x_{RC}, and x_{DC}, which are considered for varying the flow conditions. $\Delta U_{\max}$ is the maximum values of ΔU in the vertical direction (the flow near the wall is excluded) at the streamwise location of the hot wire. The table

also shows u_{rms}, longitudinal velocity integral length scale L_u, Taylor microscale λ, turbulent Reynolds number $Re_\lambda = u_{\mathrm{rms}}\lambda/\nu$, and turbulent Mach number $M_{\mathrm{T}} = u_{\mathrm{rms}}/a_0$ at the location where ΔU_{max} are obtained. Because of low M_{T}, the effects of the velocity fluctuations on shock can be evaluated apart from those of the density and temperature fluctuations. For the grid turbulence and laminar flow, ΔU_{max} is equal to 0, and u_{rms} and L_u are taken at $h = 75$ [mm]. ΔU_{max} are obtained in the RC wake for the single-cylinder experiment and in the DC wake for the double-cylinder experiments. In the double-cylinder experiment, the rms velocity fluctuation at the streamwise location of the probe is larger behind the DC wake than the RC wake.

TABLE 4.1: Experimental conditions of interaction between a spherical shock wave and a single-cylinder wake, a double-cylinder wake, grid turbulence, and a laminar flow. u_{rms} is the value at the point where ΔU_{max} is obtained.

Flow	Symbol	x_{RC} [mm]	x_{DC} [mm]	x_{G} [mm]	ΔU_{max} [m/s]	u_{rms} [m/s]
Single-cylinder wake	△	500	-	-	1.2	0.61
Double-cylinder wake	○	500	150	-	2.8	1.0
Double-cylinder wake	●	500	200	-	2.7	0.86
Double-cylinder wake	⊙	500	300	-	2.1	0.74
Grid turbulence	□	-	-	1405	0	0.56
Laminar flow	×	-	-	-	0	0.059

Flow	Symbol	L_u [mm]	λ [mm]	Re_λ	M_{T}
Single-cylinder wake	△	45	3.0	120	1.8×10^{-3}
Double-cylinder wake	○	27	1.4	100	3.0×10^{-3}
Double-cylinder wake	●	31	2.1	120	2.5×10^{-3}
Double-cylinder wake	⊙	37	2.7	140	2.2×10^{-3}
Grid turbulence	□	54	3.9	150	1.7×10^{-3}

4.3 Results and Discussion

4.3.1 Overpressure characteristics

The statistics of the peak-overpressure Δp caused by the shock wave are investigated. The definition of Δp is same as in Chapters 2 and 3. Ensemble averages of Δp, $\langle \Delta p \rangle$, are shown in Figs. 4.5(a) and (b), against the maximum values of the velocity difference, $\Delta U_{\max}$ and u_{rms}, respectively. Note that $\Delta U_{\max}$ and u_{rms} are taken at the same location. Comparison between the single-cylinder and grid turbulence experiments indicates that the non-uniform mean velocity profile in the wake results in decrease in $\langle \Delta p \rangle$. Furthermore, introducing the DC below the RC also decreases $\langle \Delta p \rangle$ as found from single- and double-cylinder experiments. It is remarkable that there is almost no difference in $\langle \Delta p \rangle$ between the grid turbulence and laminar flow cases although the grid turbulence has much stronger velocity fluctuations than the laminar flow (Tab. 4.1). This result indicates that mean shear arising from the non-uniform mean velocity in the cylinder wake has more significant effects on $\langle \Delta p \rangle$ than the velocity fluctuation. The decrease in $\langle \Delta p \rangle$ by the mean velocity defect can be explained with the effect of surface deformation of shock front propagating in a nonuniform medium (Whitham, 1958). As shown in Fig. 4.4(a), the overpressure behind the shock wave with the convex surface is known to decrease as it propagates since the ray tube area of the shock wave becomes larger as it propagates (Whitham, 1957). The fluid velocity in the streamwise direction is opposed to the propagation direction of the shock wave propagating toward the pressure measurement location as shown in Fig. 4.1(a). Since the mean streamwise velocity in the wake is smaller than outside the wake because of the velocity defect, the shock moves faster in the cylinder wake, resulting

in the convex shock surface in the shock propagating direction. As expected from the relation between the shock surface shape and overpressure discussed above, the velocity defect of the wake results in decrease in $\langle \Delta p \rangle$.

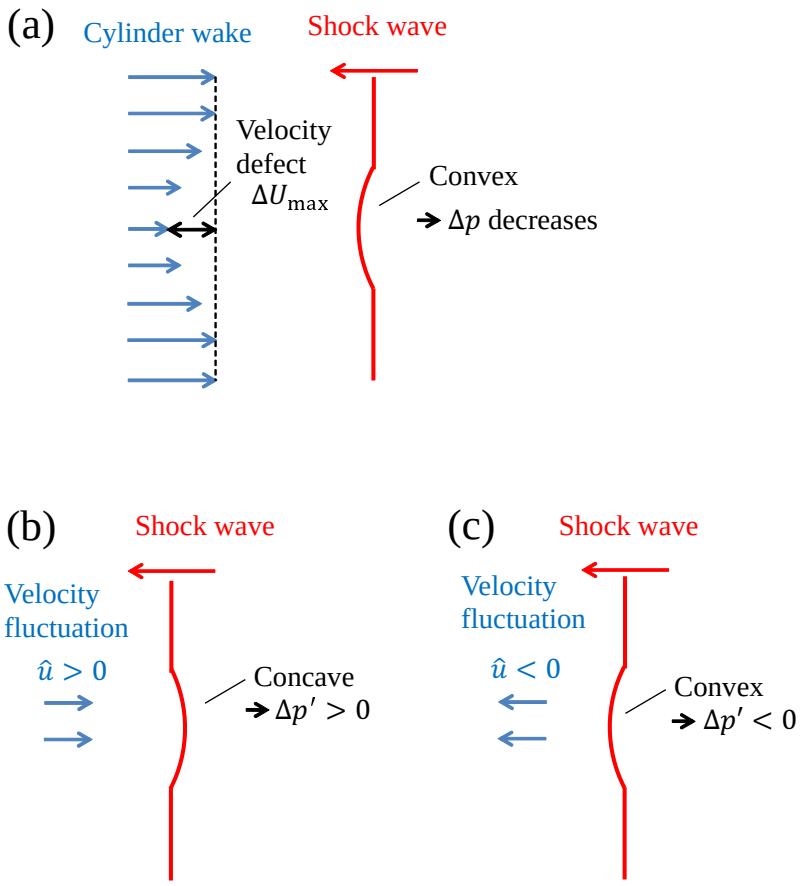

FIGURE 4.4: Schematics of shock deformation caused by (a) mean velocity defect, (b) positive velocity fluctuation, and (c) negative velocity fluctuation.

The rms peak-overpressure fluctuation $\Delta p'_{\mathrm{rms}} = \sqrt{\langle \Delta p'^2 \rangle}$ ($\Delta p' = \Delta p - \langle \Delta p \rangle$) divided by $\langle \Delta p \rangle$ is plotted against ΔU_{max} in Fig. 4.6(a) similarly to Fig. 4.5. The flow in our wind tunnel has u_{rms} of 0.059 m/s in the laminar flow at U_0 of 10 m/s. The relative intensity 0.59 % is as small as that in other wind tunnel (Seoud and Vassilicos, 2007). However, since the shock wave generator cannot produce exactly the same shock wave because of the limitation of the reproducibility, and there exists electrical noise that is inherent in the measurement system, $\Delta p'_{\mathrm{rms}}/\langle \Delta p \rangle$ of 0.016 is caused even

in the laminar flow case. In the single-cylinder experiment, $\Delta p'_{\mathrm{rms}}/\langle\Delta p\rangle$ is increased by a factor of 2.07 from the laminar case. Similar values of $\Delta p'_{\mathrm{rms}}/\langle\Delta p\rangle$ are obtained for the single-cylinder and grid turbulence, suggesting that the mean velocity profile is not directly related to the increase in $\Delta p'_{\mathrm{rms}}/\langle\Delta p\rangle$. In Fig. 4.6(b), $\Delta p'_{\mathrm{rms}}/\langle\Delta p\rangle$ is plotted against u_{rms} at the location of ΔU_{max}. $\Delta p'_{\mathrm{rms}}/\langle\Delta p\rangle$ tends to increase with u_{rms}, consistent with previous studies (Lipkens and Blackstock, 1998b; Sasoh et al., 2014). The shock wave in the double-cylinder experiments interacts with the DC wake after it passes the RC wake, where $\Delta p'_{\mathrm{rms}}/\langle\Delta p\rangle$ is larger than in the single cylinder experiment, and the DC wake contributes to the increase in $\Delta p'_{\mathrm{rms}}/\langle\Delta p\rangle$. The turbulent wake in the single cylinder experiment exists only behind the cylinder while the grid turbulence is formed in the entire wind tunnel. The grid turbulence and single-cylinder wake have a similar level of rms velocity fluctuation, and $\Delta p'_{\mathrm{rms}}/\langle\Delta p\rangle$ is also similar for both flows even though the spatial distribution of the turbulent region and mean velocity profile are different. Figures 4.5(a) and 4.6(b) also show the results obtained by 200 runs (25 runs for the laminar flow case) with gray symbols, where we can confirm that the differences from the results by 500 runs are small and that the above discussions on the statistics by 500 runs are reliable.

4.3.2 Correlation coefficients

The correlation coefficients between streamwise velocity fluctuations and peak-overpressure fluctuations are calculated as in Chapter 3. The Taylor hypothesis and low pass filter are used for calculating $\overline{U}(d,\Delta d)$ with the same method presented in Chapter 3. In the case of the cylinder wake, the convective velocity in the Taylor hypothesis is calculated as the time averaged velocity U_{ave} at the hot wire location. Here, d is defined

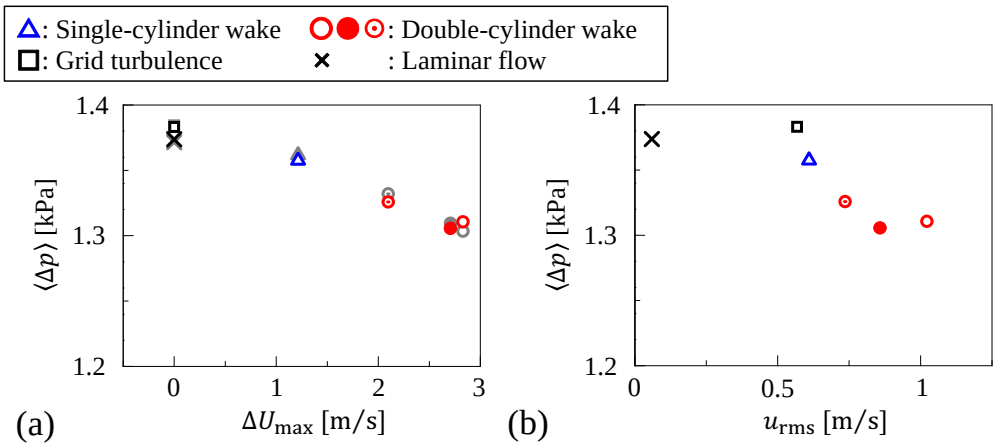

FIGURE 4.5: Relation between (a) $\langle \Delta p \rangle$ and $\Delta U_{\max}$, and (b) $\langle \Delta p \rangle$ and u_{rms}, where u_{rms} is taken at the same location as $\Delta U_{\max}$. Gray symbols in (a) are the results of 200 runs (25 runs for the laminar case).

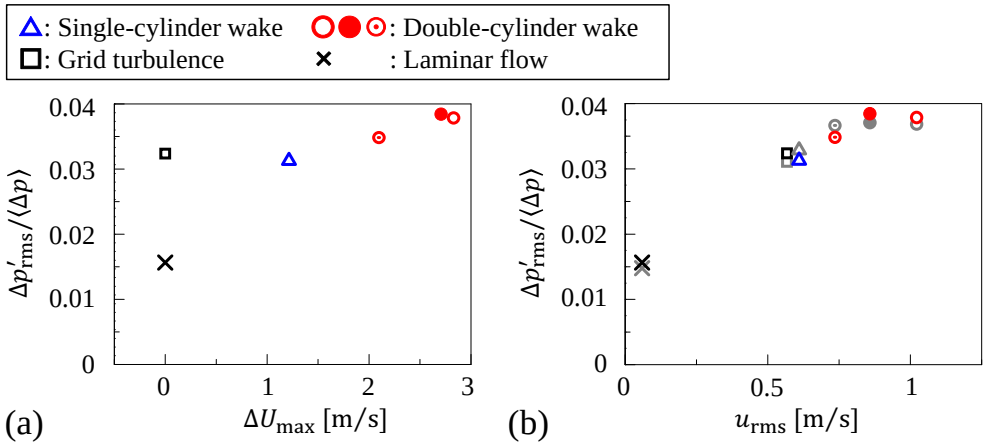

FIGURE 4.6: Relation between (a) $\Delta p'_{\mathrm{rms}}/\langle \Delta p \rangle$ and $\Delta U_{\max}$, and (b) $\Delta p'_{\mathrm{rms}}/\langle \Delta p \rangle$ and u_{rms}, where u_{rms} is taken at the same location as $\Delta U_{\max}$. Gray symbols in (b) are the results of 200 runs (25 runs for the laminar case).

as the streamwise distance from the pressure transducer location in Fig. 4.1, and Δd is the cutoff length of the low pass filter defined by Eq. (3.2). The correlation coefficients between streamwise velocity fluctuations and peak-overpressure fluctuations are calculated with Eq. (3.5).

Figure 4.7(a) shows $R(d,\Delta d)$ in the single-cylinder experiment. Large positive values of $R(d,\Delta d)$ are obtained around the peak denoted by $R_{\max}(d,\Delta d) = R(d_{\max},\Delta d_{\max})$, which is marked with a cross symbol in the figure. $R_{\max}$, $d_{\max}$, $\Delta d_{\max}$ in each flow case are summarized in Tab. 4.2. The positive correlation is consistent with the results in Chapter 3. This positive correlation between the velocity and the peak-overpressure was explained by the deformation of shock wave surface by turbulence described in Chapter 2. In the present experimental setup, a positive velocity fluctuation is opposed to the direction of the shock propagation. Then, as discussed in relation to the mean flow defect and mean peak-overpressure, the positive velocity fluctuation tends to create a concave shape on the shock wave surface, which causes the peak overpressure to increase (see Fig. 4.4(b)). Negative fluctuations are related to a convex shape with a lower peak overpressure than average (see Fig. 4.4(c)). Thus, the correlation between $\hat{u}$ and $\Delta p'$ is positive.

Figures 4.7(b), (c), and (d) show $R(d,\Delta d)$ of the double-cylinder experiments. Note that the correlation is computed for the velocity fluctuation in the RC wake, which exists above the DC wake as shown in Fig. 4.1. Comparison between Fig. 4.7(a) and Figs. 4.7(b,c,d) shows that the DC wake results in weaker correlation between the velocity fluctuation of the RC wake and the peak-overpressure fluctuation. $d_{\max}$ is compared with the shock ray in Fig. 4.8. The result from the grid turbulence experiment is also plotted in the figure. $d_{\max}$ appears around the shock ray toward the pressure measurement location $(d,h) = (0,0)$, and the turbulent velocity fluctuation near the ray is found to have a significant influence on the overpressure fluctuation.

In Fig. 4.9, $\Delta d_{\max}/L_u$ is plotted against $u_{\rm rms}$ at $h = 25$ [mm], which is below the RC wake (the height of the DC). L_u is taken at $h = 75$ [mm] (behind the RC for

the cylinder wakes) since the correlation that provides $\Delta d_{\max}/L_u$ is also computed at $h = 75$ [mm]. Here, $u_{\rm rms}$ is taken from h of the DC wake in order to investigate the effect of the DC wake on the peak-overpressure fluctuation. $\Delta d_{\max}$ are of the order of an integral length scale, confirming that the peak-overpressure fluctuation is related to large-scale motions of turbulence although the vertical distribution of turbulence is different among the experiments. In Fig. 4.10, $R_{\max}$ is plotted against $u_{\rm rms}$ at $h = 25$ [mm]. Note that $R_{\max}$ is calculated between the velocity fluctuations of RC wake (at $h = 75$ [mm]) and overpressure fluctuations, which represents the influence of RC wake on the overpressure. Therefore, the influence of DC wake on the overpressure can be evaluated by the comparison of $R_{\max}$ obtained with different $u_{\rm rms}$ of DC wake. $R_{\max}$ decreases from 0.299 to 0.165 as $u_{\rm rms}$ at $h = 25$ [mm] increases. This confirms that the influence of turbulence at $h = 75$ [mm] on the peak overpressure is weakened by the turbulence at $h = 25$ [mm]. However, $R_{\max}$ does not reach 0 even for higher $u_{\rm rms}$ at $h = 25$ [mm], and the effect of turbulence at $h = 75$ [mm] still remains on the peak overpressure. In the grid turbulence, $u_{\rm rms}$ is independent of h. Thus, the ratio of $u_{\rm rms}$ between $h = 25$ [mm] and 75]mm] is equal to 1. However, $R_{\max} = 0.275$ for the grid turbulence is similar to the value in the single-cylinder experiment, where a quasi-laminar flow exists at $h = 25$ [mm]. Thus, a turbulent region hardly weakens the influence of another turbulent region on the shock wave when these two turbulent regions have a similar level of turbulent intensity.

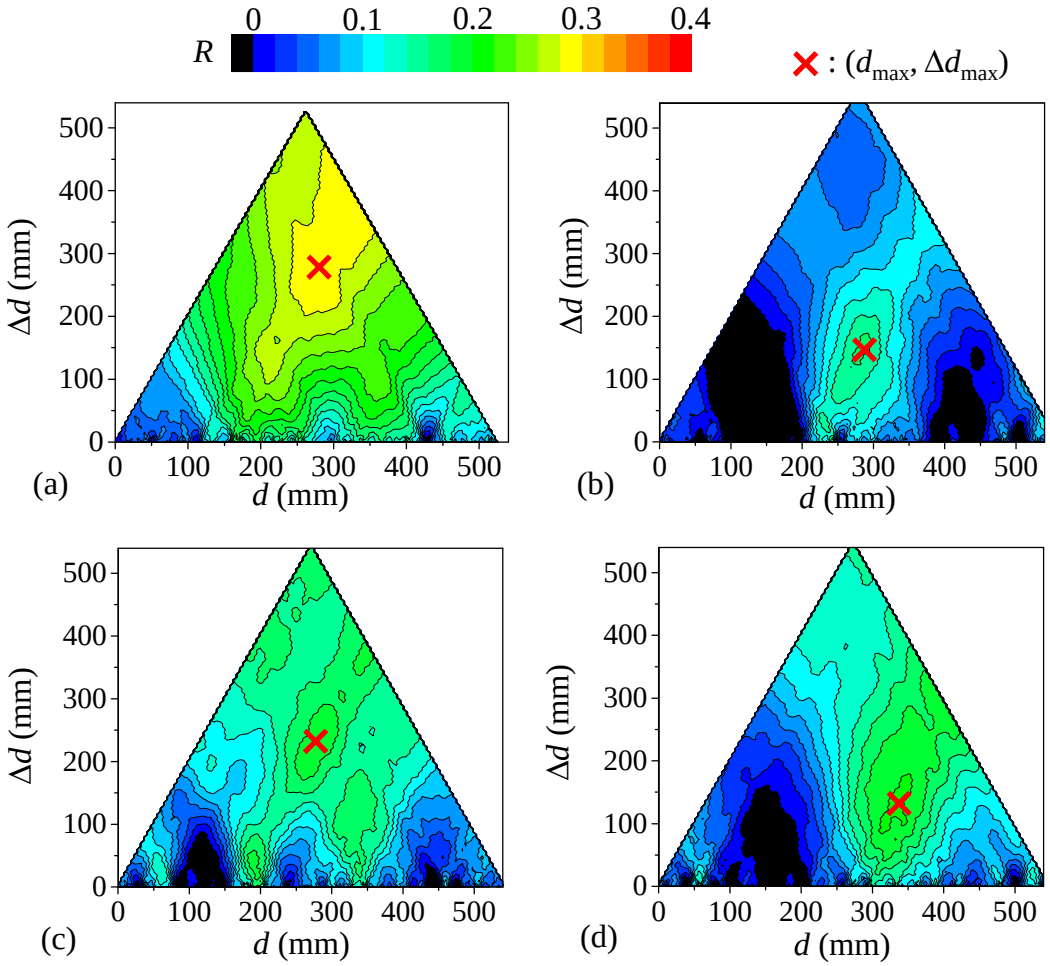

FIGURE 4.7: Correlation coefficients $R(d,\Delta d)$ between the peak-overpressure fluctuation and velocity fluctuation in (a) single-cylinder experiment and double-cylinder experiment with (b) $x_{DC} = 150$ [mm], (c) $x_{DC} = 200$ [mm], and (d) $x_{DC} = 300$ [mm]. The crosses show $(d,\Delta d) = (d_{max},\Delta d_{max})$, where R has a maximum value R_{max} in each figure.

4.4 Summary of this chapter

The experiments on the interaction between the spherical shock wave and turbulence in a wind tunnel have been conducted, and the overpressure behind the shock wave and the fluid velocity have been measured simultaneously. The experiments have been performed with a single-cylinder wake, a double-cylinder wake, grid turbulence, and a laminar flow. The influences of these flows on the shock wave have been compared to investigate the effects of the inhomogeneity of turbulence on the shock

TABLE 4.2: $R_{\max}$, $d_{\max}$, and $\Delta d_{\max}$ in each flow case.

Flow	Symbol	$R_{\max}$	$d_{\max}$ [mm]	$\Delta d_{\max}$ [mm]
Single-cylinder wake	△	0.299	274	296
Double-cylinder wake	○	0.165	287	158
Double-cylinder wake	●	0.193	284	246
Double-cylinder wake	⊙	0.210	332	126
Grid turbulence	□	0.275	260	160

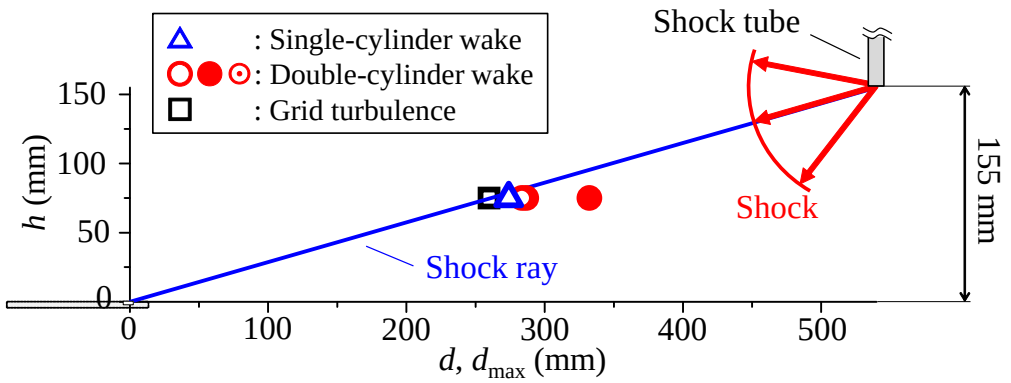

FIGURE 4.8: Comparison of $(d_{\max}, h)$ and the shock ray along which the shock wave propagates to the pressure transducer location $(d, h) = (0, 0)$.

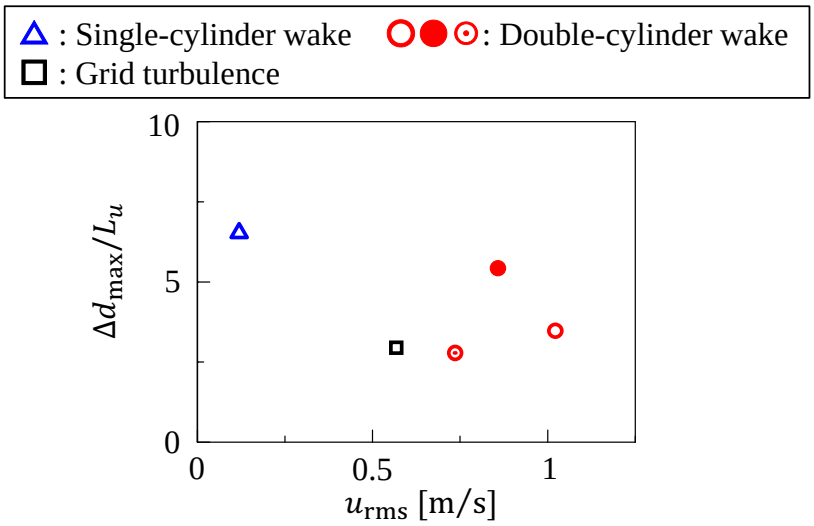

FIGURE 4.9: $\Delta d_{\max}/L_u$ plotted against $u_{\rm rms}$ at $h = 25$ [mm].

wave characteristics.

The mean peak-overpressure $\langle \Delta p \rangle$ is found to change after the shock wave passes

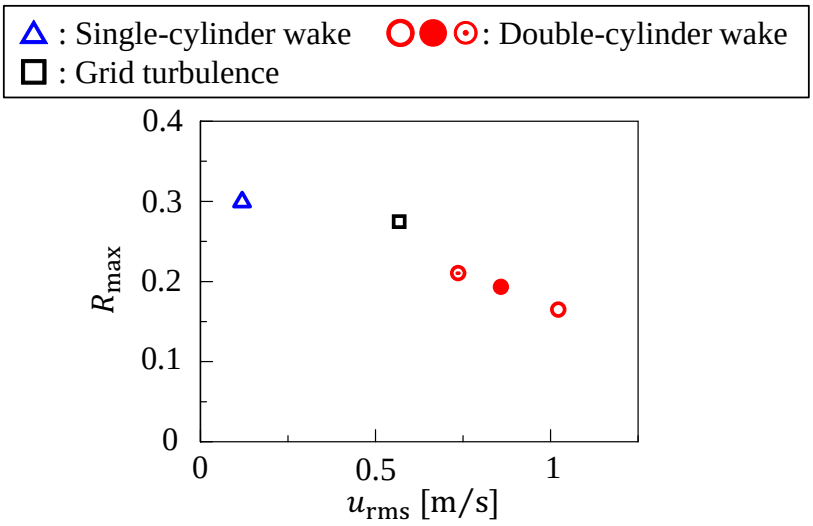

FIGURE 4.10: R_{max} plotted against u_{rms} at $h = 25$ [mm].

the flow with a non-uniform mean velocity profile such as cylinder wakes. Comparisons between experiments with the wakes, grid turbulence, and laminar flow shows that $\langle \Delta p \rangle$ is almost independent from the turbulent intensity since $\langle \Delta p \rangle$ is similar for the grid turbulence and laminar flow. The rms peak-overpressure fluctuation intensity $\Delta p'_{rms}/\langle \Delta p \rangle$, on the other hand, tends to increase with rms velocity fluctuation of turbulence that interacts with the shock wave, without a significant dependence on a mean velocity profile. Correlation coefficients are calculated between the peak-overpressure fluctuation behind the shock wave and the low-pass filtered velocity fluctuation of the turbulence. It is shown that a large-scale turbulent velocity fluctuation near the shock ray has a strong influence on the shock wave characteristics. In the double-cylinder experiments, the shock wave passes two turbulent wakes. The effects of the first wake, evaluated with the correlation coefficients between the peak-overpressure fluctuation and the low-pass filtered velocity fluctuation of the first wake, are weakened after the shock wave passes the second wake, which has a

higher rms velocity fluctuation than the first wake. This influence of the second wake is shown to be more important as its rms velocity fluctuation increases.

Chapter 5

Conclusions

In this thesis, the fundamental aspects of the shock-turbulence interaction phenomena were studied experimentally with the focus on effects of turbulent velocity fluctuations on a shock wave. Experiments of a spherical shock wave propagating through turbulence in the wind tunnel were repeatedly conducted in order to investigate the statistics of the overpressure behind a shock wave after the interaction. The physical meanings of the experimental results were also considered by constructing the theoretical model. Here, the main findings in Chapters 2 to 4 are summarized based on the objective mentioned in Chapter 1.

In Chapter 2, the overpressure fluctuations behind a shock wave caused by the interaction with turbulence were investigated, where various conditions for shock Mach number M_{S0} and turbulent Mach number M_T were considered to elucidate the relation between the overpressure and the these Mach numbers. The Gaussianity of the peak-overpressure fluctuations was found in all the experimental conditions. The rms peak-overpressure fluctuation divided by the averaged peak-overpressure was found to be increased as a function of $M_T^2/(M_{S0}^2 - 1)$. The statistical properties obtained in the experiments were well explained by a shock deformation model, where

a shock wave interacting with local velocity fluctuations was considered. This implies that shock wave deformation is an important cause of the overpressure change in the shock-turbulence interaction.

In Chapter 3, the relation between the instantaneous velocity of turbulence and the overpressure fluctuation behind a shock wave was discussed. The correlation coefficients were calculated between the velocity and peak-overpressure fluctuations. The positive correlation was obtained, which showed that the increase in the turbulent velocity fluctuation opposing to the shock propagation direction yields the increase in the overpressure fluctuation. It is remarkable that the peak overpressure was strongly correlated with the velocity of turbulence interacting at some distance away from the pressure measurement point. This means that overpressure fluctuation significantly appears some time after the shock wave interacts with turbulent velocity fluctuation, suggesting the existence of the response time of the shock wave modulation by turbulence.

The effect of inhomogeneity of velocity characteristics of turbulence on shock wave modulation was discussed in Chapter 4. The inhomogeneous turbulence was produced in the wind tunnel by introducing double cylinder wake consisting of upper and lower cylinder wakes. The interaction between the double cylinder wake and a shock wave was compared with the results of the interaction between quasi-homogeneous flow (laminar flow and grid turbulence) to the evaluation of the effects of the inhomogeneity on the shock wave. It was found that the larger the velocity defect behind the cylinder wake is, the smaller the averaged peak overpressure becomes. This is qualitatively consistent with the result of the shock deformation

model constructed in Chapter 2; the velocity defect caused in the present experiments makes the shock wave convexly deformed in the shock propagation direction, resulting in the attenuation of the shock Mach number and overpressure. Thus, the inhomogeneity in the mean-velocity profile of cylinder wake strongly affects the averaged peak overpressure. On the other hand, the rms peak overpressure was not dependent on the velocity defect, but was increased with the rms velocity fluctuation of the cylinder wake. It was also found that the correlation between the upper cylinder wake velocity and the peak-overpressure fluctuations was weakened after the shock wave interacted with the lower cylinder wake. The correlation coefficients between them decreased as the rms velocity fluctuation of the lower cylinder wake increased. Hence, by strengthening the inhomogeneity of turbulence velocity fluctuation profile, the effect of the velocity fluctuation interacting with the shock wave at a certain point on the shock ray can be changed significantly during the shock propagation.

Appendix A

Relation between Δp and $\Delta\rho$

The sound speed equation behind the shock wave is

$$a_2^2 = \frac{\gamma(\langle\Delta p\rangle + p_0)}{\langle\Delta\rho\rangle + \rho_0}. \tag{A.1}$$

According to Lee, Lele, and Moin, 1993, from the isentropic relation, the fluctuations in pressure and density jumps are related by

$$\Delta p' = a_2^2 \Delta\rho'. \tag{A.2}$$

From Eqs. (A.1) and (A.2) and the sound speed equation in front of the shock wave $a_0^2 = \gamma p_0/\rho_0$, the relation between $\Delta p'/\langle\Delta p\rangle$ and $\Delta\rho'/\langle\Delta\rho\rangle$ is obtained as follows:

$$\frac{\Delta p'}{\langle\Delta p\rangle} = \frac{\gamma\Delta\rho'}{\langle\Delta\rho\rangle + \rho_0 - \frac{\gamma p_0}{a_2^2}} = \frac{\gamma\Delta\rho'}{\langle\Delta\rho\rangle + \rho_0\left(1 - \frac{a_0^2}{a_2^2}\right)}. \tag{A.3}$$

According to the Rankine-Hugoniot relations,

$$\frac{\langle\Delta\rho\rangle}{\rho_0} = \frac{2(M_{S0}^2 - 1)}{(\gamma-1)M_{S0}^2 + 2}. \tag{A.4}$$

Equations (2.16), (A.3), and (A.4) yield

$$\frac{\Delta p'}{\langle \Delta p \rangle} = \frac{2\gamma M_{S0}^2 - \gamma + 1}{(\gamma+1)M_{S0}^2} \frac{\Delta \rho'}{\langle \Delta \rho \rangle} = m \frac{\Delta \rho'}{\langle \Delta \rho \rangle}, \tag{A.5}$$

where $m \equiv (2\gamma M_{S0}^2 - \gamma + 1)/\{(\gamma+1)M_{S0}^2\}$. The standard deviation of Eq. (A.5) yields

$$\frac{\sigma_{\Delta p}}{\langle \Delta p \rangle} = m \frac{\sigma_{\Delta \rho}}{\langle \Delta \rho \rangle}. \tag{A.6}$$

Appendix B

Shock Mach number fluctuation for a strong shock wave

For a strong shock wave ($M_{S0} \to \infty$), Eq. (2.26) can be simplified (Whitham, 1959) as

$$\frac{A}{A_0} \approx \left(\frac{M_{S0}}{M_S}\right)^n, \tag{B.1}$$

where $n = \lim_{M_S \to \infty}\{(M_S^2 - 1)g/M_S\} \approx 5.0743$. For $M_{S0} \gtrsim 2.6$, the error of the A–M_S relation calculated with Eq. (B.1) from that calculated with Eq. (2.26) is within 10%. From Eqs. (2.25) and (B.1), M_S' is written as

$$M_S' \approx \frac{1-(2\xi+1)^{1/n}}{(2\xi+1)^{1/n}} M_{S0} \approx -\frac{2}{n}\xi M_{S0}, \tag{B.2}$$

where $(2\xi+1)^{1/n} \approx 2\xi/n + 1$ ($\xi \ll 1$) is used for small deformation. Differentiation of both sides of Eq. (B.2) with respect to x_R yields

$$\frac{dM_S'}{dx_R} \approx -\frac{2M_{S0}}{n}\frac{u + a_0 M_S'/2}{U_{S0}\tan\alpha}\frac{1}{r_0}. \tag{B.3}$$

The solution of Eq. (B.3) is

$$M'_{\mathrm{S}} \approx -\frac{2u}{a_0}\left[1-\exp\left(-\frac{1}{n\tan\alpha}\frac{x_{\mathrm{R}}}{r_0}\right)\right]. \tag{B.4}$$

Therefore, $M'_{\mathrm{S}l} \equiv M'_{\mathrm{S}}(x_l)$ is

$$M'_{\mathrm{S}l} \approx -\frac{2u}{a_0}\left[1-\exp\left(-\frac{1}{n\tan\alpha}\right)\right] = -c\frac{u}{a_0}, \tag{B.5}$$

where $x_l/r_0 \approx 1$ is used and c is defined as $c \equiv 2\left[1-\exp\left(-\frac{1}{n\tan\alpha}\right)\right]$. From Eqs. (2.38), (2.40), and (B.5), $\Delta p'/\langle\Delta p\rangle$ for $M_{\mathrm{S0}} \to \infty$ is written as

$$\frac{\Delta p'}{\langle\Delta p\rangle} \approx -\frac{2M_{\mathrm{S0}}}{M_{\mathrm{S0}}^2-1}c\frac{u}{a_0} \approx -2c\frac{u/a_0}{M_{\mathrm{S0}}}. \tag{B.6}$$

Since $c \approx 0.7658$ for $M_{\mathrm{S0}} \to \infty$, we have

$$\frac{\Delta p'}{\langle\Delta p\rangle} \approx -1.532\frac{u/a_0}{M_{\mathrm{S0}}}. \tag{B.7}$$

The standard deviations of Eq. (B.7) yield the following relation among $\sigma_{\Delta p}/\langle\Delta p\rangle$, M_{S0}, and M_{T}:

$$\frac{\sigma_{\Delta p}}{\langle\Delta p\rangle} \sim \frac{M_{\mathrm{T}}}{M_{\mathrm{S0}}}. \tag{B.8}$$

References

Agostini, L., L. Larchevêque, and P. Dupont (2015). "Mechanism of shock unsteadiness in separated shock/boundary-layer interactions". In: *Phys. Fluids* 27.12, p. 126103.

Agui, J. H., G. Briassulis, and Y. Andreopoulos (2005). "Studies of interactions of a propagating shock wave with decaying grid turbulence: velocity and vorticity fields". In: *J. Fluid Mech.* 524, pp. 143–195.

Andreopoulos, Y., J. H. Agui, and G. Briassulis (2000). "Shock wave-turbulence interactions". In: *Ann. Rev. Fluid Mech.* 32.1, pp. 309–345.

Barre, S., D. Alem, and J. P. Bonnet (1996). "Experimental study of a normal shock/homogeneous turbulence interaction". In: *AIAA J.* 34.5, pp. 968–974.

Ben-Dor, G. (1992). *Shock wave reflection phenomena*. Springer.

Burlaga, L. F. et al. (2006). "Tsallis statistics of the magnetic field in the heliosheath". In: *ApJ Lett.* 644.1, p. L83.

Bushnell, D. M. (2004). "Shock wave drag reduction". In: *Annu. Rev. Fluid Mech.* 36, pp. 81–96.

Carlson, H. W. (1967). "Experimental and analytical research on sonic boom generation at NASA". In: *NASA SP* 147, p. 9.

Chen, C. H. and D. A. Donzis (2019). "Shock–turbulence interactions at high turbulence intensities". In: *J. Fluid Mech.* 870, pp. 813–847.

Chisnell, R. F. (1957). “The motion of a shock wave in a channel, with applications to cylindrical and spherical shock waves”. In: *J. Fluid Mech.* 2.3, pp. 286–298.

Clavin, P. (2013). “Nonlinear analysis of shock–vortex interaction: Mach stem formation”. In: *J. Fluid Mech.* 721, pp. 324–339.

Delery, J. M. (1985). “Shock wave/turbulent boundary layer interaction and its control”. In: *Prog. Aerospace Sci.* 22.4, pp. 209–280.

Dokukina, O. I. et al. (2013). “Pressure fluctuations within a turbulent gas flow and their interaction with a shock wave”. In: *Mosc. Univ. Phys. Bull.* 68.2, pp. 118–122.

Dolling, D. S. (2001). “Fifty years of shock-wave/boundary-layer interaction research: what next?” In: *AIAA J.* 39.8, pp. 1517–1531.

Donzis, D. A. (2012a). “Amplification factors in shock-turbulence interactions: Effect of shock thickness”. In: *Phys. Fluids* 24.1, p. 011705.

— (2012b). “Shock structure in shock-turbulence interactions”. In: *Phys. Fluids* 24, p. 126101.

Dosanjh, D. S. (1956). “Interaction of grids with traveling shock waves”. In: *NACA TN-3680*.

Fang, X. et al. (2018). “Effects of oblique shock waves on turbulent structures and statistics of supersonic mixing layers”. In: *Phys. Fluids* 30.11, p. 116101.

Friedlander, F. G. (1946). “The diffraction of sound pulses I. Diffraction by a semi-infinite plane”. In: *Proc. R. Soc. Lond. A* 186.1006, pp. 322–344.

Fujino, Kuninori et al. (2017). “Effects of uncertainties in atmospheric turbulence and weather predictions on sonic boom”. In: *Proc. 55th AIAA Aerospace Sciences Meeting*, p. 0280.

Giacalone, J. and J. R. Jokipii (2007). “Magnetic field amplification by shocks in turbulent fluids”. In: *ApJ Lett.* 663.1, p. L41.

Gnani, F., H. Zare-Behtash, and K. Kontis (2016). “Pseudo-shock waves and their interactions in high-speed intakes”. In: *Prog. Aerospace Sci.* 82, pp. 36–56.

Grasso, F. and S. Pirozzoli (2000). “Shock-wave–vortex interactions: shock and vortex deformations, and sound production”. In: *Theor. Comput. Fluid Dyn.* 13.6, pp. 421–456.

Honda, M. and K. Yoshida (2012). “D-SEND project for low sonic boom design technology”. In: *28th International Congress of the Aeronautical Sciences*.

— (2014). “D-SEND #2 flight demonstration for low sonic boom design technology”. In: *Proceedings of ICAS 2014*.

Jeong S.and Ono, D., K. Shimoyama, and A. Hashimoto (2013). “Sonic boom analysis under conditions of atmospheric uncertainty using polynomial chaos”. In: *Trans. Japan Soc. Aero. Space Sci.* 56.3, pp. 129–136.

Keller, J and W Merzkirch (1994). “Interaction of a normal shock wave with a compressible turbulent flow”. In: *Mineralium Deposita* 29.1, pp. 241–248.

Kim, J. H., A. Sasoh, and A. Matsuda (2010). “Modulations of a weak shock wave through a turbulent slit jet”. In: *Shock Waves* 20.4, pp. 339–345.

Kitamura, T. et al. (2014). “On invariants in grid turbulence at moderate Reynolds numbers”. In: *J. Fluid Mech.* 738, pp. 378–406.

Kitamura, T. et al. (2016). “Rapid distortion theory analysis on the interaction between homogeneous turbulence and a planar shock wave”. In: *J. Fluid Mech.* 802, pp. 108–146.

Kitamura, T et al. (2017). “Changes in divergence-free grid turbulence interacting with a weak spherical shock wave”. In: *Phys. Fluids* 29.6, p. 065114.

Krogstad, P.-Å. and P. A. Davidson (2010). “Is grid turbulence Saffman turbulence?” In: *J. Fluid Mech.* 642, pp. 373–394.

Lahiri, S. K. and L. Ho (2011). “Simulation of rapid structural failure due to blast loads from conventional weapons (CONWEP)”. In: *Proceedings of the NAFEMS World Congress*.

Landau, L. D. (1945). “On shock waves at large distances from the place of their origin”. In: *J. Phys. USSR* 9.6, pp. 496–500.

Larsson, J., I. Bermejo-Moreno, and S. K. Lele (2013). “Reynolds- and Mach-number effects in canonical shock-turbulence interaction”. In: *J. Fluid Mech.* 717, pp. 293–321.

Larsson, J. and S. K. Lele (2009). “Direct numerical simulation of canonical shock/turbulence interaction”. In: *Phys. Fluids* 21.12, p. 126101.

Lee, S., S. K. Lele, and P. Moin (1993). “Direct numerical simulation of isotropic turbulence interacting with a weak shock wave”. In: *J. Fluid Mech.* 251, pp. 533–562.

Lele, S. K. (1992). “Shock-jump relations in a turbulent flow”. In: *Phys. Fluids* 4.12, pp. 2900–2905.

Li, N. et al. (2017). “Prediction dynamic model of shock train with complex background waves”. In: *Phys. Fluids* 29.11, p. 116103.

Liang, S. M., J. S. Wang, and H. Chen (2002). “Numerical study of spherical blast-wave propagation and reflection”. In: *Shock Waves* 12.1, pp. 59–68.

Lipkens, B. and D. T. Blackstock (1998a). "Model experiment to study sonic boom propagation through turbulence. Part I. General results". In: *J. Acoust. Soc. Am.* 103.1, pp. 148–158.

— (1998b). "Model experiment to study sonic boom propagation through turbulence. Part II. Effect of turbulence intensity and propagation distance through turbulence". In: *J. Acoust. Soc. Am.* 104.3, pp. 1301–1309.

Lipkens, Bart and David T Blackstock (1998c). "Model experiment to study sonic boom propagation through turbulence. Part I: General results". In: *J. Acoust. Soc. Am.* 103.1, pp. 148–158.

Mac Low, M.-M. and R. S. Klessen (2004). "Control of star formation by supersonic turbulence". In: *Rev. Mod. Phys.* 76.1, p. 125.

Maglieri, D. J. (1966). "Some effects of airplane operations and the atmosphere on sonic-boom signatures". In: *J. Acoust. Soc. Am.* 39.5B, S36–S42.

Maglieri, D. J. et al. (2014). "Sonic boom: Six decades of research". In: *NASA SP-2014-622*.

Needham, C. E. (2010). *Blast waves*.

Nieuwstadt, F. T. M., J. Westerweel, and B. J. Boersma (2016). *Turbulence: introduction to theory and applications of turbulent flows*. Springer.

Osaka, Hideo et al. (1983). "The structure of a turbulent wake behind a cruciform circular cylinder: 2nd report, the streamwise development of turbulent flow field". In: *Jpn. Soc. Mech. Eng.* 26.214, pp. 521–528.

Ozawa, H. (2016). "Experimental study of unsteady aerothermodynamic phenomena on shock-tube wall using fast-response temperature-sensitive paints". In: *Phys. Fluids* 28.4, p. 046103.

Pepper, C. B., M. A. Nascarella, and R. J. Kendall (2003). “A review of the effects of aircraft noise on wildlife and humans, current control mechanisms, and the need for further study”. In: *Environ. Manage.* 32.4, pp. 418–432.

Piacsek, A. A. (2002). “Atmospheric turbulence conditions leading to focused and folded sonic boom wave fronts”. In: *J. Acoust. Soc. Am.* 111.1, pp. 520–529.

Pierce, A. D. (1971). “Statistical theory of atmospheric turbulence effects on sonic-boom rise times”. In: *J. Acoust. Soc. Am.* 49.3B, pp. 906–924.

Plotkin, K. J. and A. R. George (1972). “Propagation of weak shock waves through turbulence”. In: *J. Fluid Mech.* 54.3, pp. 449–467.

Poggi, F., M.-H. Thorembey, and G. Rodriguez (1998). “Velocity measurements in turbulent gaseous mixtures induced by Richtmyer–Meshkov instability”. In: *Phys. Fluids* 10.11, pp. 2698–2700.

Pope, S. B. (2001). *Turbulent flows*.

Ribner, H. S. (1954). “Convection of a pattern of vorticity through a shock wave”. In: *NACA Report No. 1164*.

— (1955). “Shock-turbulence interaction and the generation of noise”. In: *NACA Report No. 1233*.

Ribner, H. S., P. J. Morris, and W. H. Chu (1973). “Laboratory simulation of development of superbooms by atmospheric turbulence”. In: *J. Acoust. Soc. Am.* 53.3, pp. 926–928.

Ryu, J. and D. Livescu (2014). “Turbulence structure behind the shock in canonical shock–vortical turbulence interaction”. In: *J. Fluid Mech.* 756.

Salze, E. et al. (2014). “Laboratory-scale experiment to study nonlinear N-wave distortion by thermal turbulence”. In: *J. Acoust. Soc. Am.* 136.2, pp. 556–566.

Sasoh, A., K. Takayama, and T. Saito (1992). "A weak shock wave reflection over wedges". In: *Shock Waves* 2.4, pp. 277–281.

Sasoh, A. et al. (2014). "Statistical behavior of post-shock overpressure past grid turbulence". In: *Shock Waves* 24.5, pp. 489–500.

Schwer, L. (2017). "Air blast reflection ratios and angle of incidence". In: *Proceedings of the 11th European LS-DYNA Conference, Salzburg, Austria*, pp. 9–11.

Seegmiller, H. L., J. G. Marvin, and L. L. Levy Jr. (1978). "Steady and unsteady transonic flow". In: *AIAA J.* 16.12, pp. 1262–1270.

Seoud, R. E. and J. C. Vassilicos (2007). "Dissipation and decay of fractal-generated turbulence". In: *Phys. Fluids* 19.10, p. 105108.

Sethuraman, Y. P. M. and K. Sinha (2020). "Effect of turbulent Mach number on the thermodynamic fluctuations in canonical shock-turbulence interaction". In: *Comput. Fluids*, p. 104354.

Tamba, T. et al. (2015a). "Counter-driver shock tube". In: *Shock Waves* 25.6, pp. 667–674.

Tamba, T. et al. (2015b). "Frequency modulation in shock wave-boundary layer interaction by repetitive-pulse laser energy deposition". In: *Phys. Fluids* 27.9, p. 091704.

Tamba, T. et al. (2016). "Field experiment of blast wave pressure modulation past a turbulent flow". In: *Sci. Tech. Energetic Materials* 77.3-4, pp. 91–97.

Tamba, T. et al. (2019). "Experimental investigation of the interaction of a weak planar shock with grid turbulence in a counter-driver shock tube". In: *Phys. Rev. Fluids* 4.7, p. 073401.

Tanaka, K. et al. (2018). “Amplification and attenuation of shock wave strength caused by homogeneous isotropic turbulence”. In: *Phys. Fluids* 30.3, p. 035105.

Thomas, V. A. and R. J. Kares (2012). “Drive asymmetry and the origin of turbulence in an ICF implosion”. In: *Phys. Rev. Lett.* 109.7, p. 075004.

Whitham, G. B. (1957). “A new approach to problems of shock dynamics Part 1 Two-dimensional problems”. In: *J. Fluid Mech.* 2.02, pp. 145–171.

— (1958). “On the propagation of shock waves through regions of non-uniform area or flow”. In: *J. Fluid Mech.* 4.04, pp. 337–360.

— (1959). “A new approach to problems of shock dynamics Part 2. Three-dimensional problems”. In: *J. Fluid Mech.* 5.3, pp. 369–386.

Yamashita, H. and S. Obayashi (2009). “Sonic boom variability due to homogeneous atmospheric turbulence”. In: *J. Aircraft* 46.6, pp. 1886–1893.

Zhuang, Y. et al. (2018). “Görtler-like vortices in an impinging shock wave/turbulent boundary layer interaction flow”. In: *Phys. Fluids* 30.6, p. 061702.